

# Spike-frequency and h-current based adaptation are dynamically equivalent in a Wilson-Cowan field model

Ronja Strömsdörfer<sup>1,2,\*</sup> and Klaus Obermayer<sup>1,2,3</sup>

<sup>1</sup>*Neural Information Processing Group, Fakultät IV, Technische Universität Berlin, Berlin, Germany*

<sup>2</sup>*Einstein Center for Neuroscience, Berlin, Germany*

<sup>3</sup>*Bernstein Center for Computational Neuroscience, Berlin, Germany*

(Dated: October 16, 2025)

During slow-wave sleep, the brain produces traveling waves of slow oscillations (SOs;  $\leq 2$  Hz), characterized by the propagation of alternating high- and low-activity states. They play a crucial role in memory consolidation and are frequently investigated, empirically and with the support of in-silico studies. The question of internal mechanisms that modulate traveling waves of SOs is still unanswered even though it is established that it is an adaptation mechanism that mediates them. One of the main mechanisms investigated is spike-frequency adaptation (SFA), a hyperpolarizing feedback current that is activated during periods of high-activity. An alternative mechanism which has recently been suggested is based on hyperpolarization-activated (h-)currents, which are positive feedback currents that are activated in low-activity states. Both adaptation mechanisms were shown to feature SO-like dynamics in neuronal populations, and the inclusion of a spatial domain seems to enhance observable differences in their effects. To investigate the effects of both adaptation mechanisms on the neural dynamics in detail, we examine a spatially extended, adaptive Wilson-Cowan model of interacting excitatory and inhibitory populations of neurons with local spatial coupling. The excitatory populations are equipped with either one or the other adaptation mechanism. We describe both mechanisms using the same dynamical equation and include the inverse mode of action by changing the signs of the adaptation strength and the gain of activation function. We then show that the dynamical systems including the two feedback currents are mathematically equivalent under a compensatory external input, which depends on the adaptation strength and which in turn leads to a shift in state space of the otherwise equivalent bifurcation structure. A detailed analysis of state space shows that strong enough adaptation is required to induce traveling waves of SO-like dynamics while only stationary or homogeneous activity patterns emerge if adaptation is weak. Additionally, adaptation modulates the properties of the spatio-temporal activity patterns, such as temporal frequencies, spatial frequencies, and the speed of the traveling waves, all of which increase with increasing strength. Though being dynamically equivalent, our results also explain why location-dependent variations in feedback strength cause differences in the propagation of traveling waves between both adaptation mechanisms.

## I. INTRODUCTION

One of the most frequently investigated rhythms in the brain is the phenomenon of slow oscillations (SOs), which appear during slow-wave sleep and are characterized by the slow alternation of high- and low-activity states, also referred to as up- and down-states [1, 2]. They were first described by [3]<sup>1</sup>, and have been shown to play a crucial role in memory consolidation since then [5–7]. On a mesoscopic scale, SOs tend to travel in wave-like patterns across the cortex [8]. Due to their dominant temporal frequency being below  $\leq 1$  Hz, SOs are most likely driven by an adaptation process which acts on a slower time scale than the standard neuronal response. Nonetheless, the exact nature and dynamics of the adaptation mechanism are still in question.

One candidate process is spike-frequency adaptation (SFA), a hyperpolarizing feedback current (i.e., a neg-

ative feedback mechanism) induced by ongoing high-activity in neuronal populations which is often mediated by slow potassium ( $K^+$ ) currents (see [9, 10]). Since the neurotransmitter acetylcholine (ACh) decreases  $K^+$  conductance [11] and since ACh concentration is lower during natural sleep compared to wakefulness [12], SFA is elevated during sleep. Comparing different species, two types of slow waves were separated in [13] depending on whether they occur in natural slow-wave sleep or whether they occur under anesthesia. [14] reported that the durations of up-states following down-states are positively correlated during anesthesia in rats, while [13] observed a negative correlation, with long down-states being followed by short up-states in natural sleep in several species. In [13], reduced cholinergic modulation (i.e., lowered ACh concentration) increased the incidence of short up-states subsequent to long down-states, thereby recapitulating both the slow-wave patterns of natural sleep and the neuromodulatory effects of varying ACh concentrations in the sleeping brain.

Hyperpolarization-activated h-currents (i.e., a positive feedback mechanism) have also been shown to slowly modulate neuronal excitability (see [15]) and may also cause adaptation-driven traveling waves similar to cor-

\* Corresponding author: stroemsdoerfer@tu-berlin.de

<sup>1</sup> Note, however, that cortical down states, which correspond to so-called K-complexes, have already been described in the very first sleep EEG studies in the 1930s [4].

tical waves of SO-like dynamics. In [16], using ferret slice experiments, it was proposed that h-current modulation regulates the cortical capacity for recurrent persistent activity, which encompasses slow-wave dynamics. Until most recently, h-currents were predominantly investigated in thalamocortical systems [17–19] which aligns with their presence in thalamic neurons [20]. However, [21], and [22] focus on the impact of h-currents on cortical slow waves, i.e., on the propagation of alternating up- and down-states over space.

Spatially extended neural field models are a convenient computational approach for investigating the propagation features of traveling waves. They inherit a description of space through spatial convolution, which effectively describes distance-dependent connectivity profiles in continuous space [23–25]. Depending on their setup, neural field models can produce periodic traveling waves [26]. For the one-population model of integrate-and-fire neurons with synaptic inputs on a continuous one-dimensional space of [27], analytical predictions align with numerical simulations showing that the speed of traveling waves fluctuates over space when there is a subset of tightly coupled neurons. In [28], traveling waves emerge in a system of quadratic integrate-and-fire neurons with nonlocal synaptic coupling as the synaptic coupling strength is increased. Generally speaking, the emergence of spatio-temporal patterns relies on the underlying dynamical state of the model system. Suitable parameterizations can be identified by a Turing instability analysis performed in the Fourier domain. This analysis is most often performed in systems comprised of either a single neural population (e.g., [29, 30]) or two coupled populations of excitatory and inhibitory neurons (e.g., [31, 32]).

One frequently used model is the Wilson-Cowan model which was first introduced in [33] in its mass model version, i.e., without a spatial domain. The mass model version displays a rich variety of emergent dynamics and has previously been used to investigate SFA-driven SOs, either with [34, 35] or without inhibition [36]. In its original form, comprising of one excitatory and one inhibitory population of neurons without SFA [37], the dynamical landscape of this model remains fairly similar when both SFA and inhibition are included, when only SFA is present, or when both are absent. A regime of oscillations (e.g., emerging due to a Hopf instability) is at the corner end of a regime of bistability, where a stable up- and down-state coexist.

To include a spatial domain, Wilson and Cowan extended the mass model to a field model which is comprised of two coupled populations of excitatory and inhibitory neurons [38]. Pinto and Ermentrout [39] investigated the system without an inhibitory population, but with a linear, negative feedback that limits the networks excitability. They establish the existence of traveling pulses in such a network and connect the speed of the waves, which are induced by the slow negative feedback, to the model parameters using the Heaviside func-

tion as transfer function. A sigmoidal transfer function speeds up waves further when compared to the Heaviside transfer function. For a homogeneous, excitatory neural field model, [40] proved that lateral inhibition is required to stabilize bump solutions (i.e., stabilize the activity to not decay or vanish over time), and while [41] confirms these findings, they additionally show that local inhomogeneous input stabilizes stationary-pulse solutions in an otherwise homogeneous network. In [42], the authors investigate the same field model without inhibition in which nonlinear negative feedback to an excitatory population of neurons is produced by synaptic depression and SFA simultaneously. They identify traveling fronts and pulses, as well as stationary or homogeneous oscillations. They show that synaptic depression is not sufficient to stabilize bump solutions and confirm that either lateral inhibition (as shown in [40]) or external input (as shown in [41]) is required. Conversely, bumps do not exist when SFA is present. Furthermore, they investigated the phase space with respect to the strengths of SFA and synaptic depression and found that SFA has little to no effect on the speed and width of traveling fronts and pulses. Their nonlinear formulation of SFA feedback is a physiologically based negative feedback. In [43], the authors equip the excitatory population of the two-population model with SFA and investigate the conditions for Turing and Hopf bifurcations to emerge, enabling stationary or spatio-temporal activity. While weaker and faster adaptation generates stationary patterns, slower and stronger adaptation causes the stationary patterns to travel.

Now, we are left with the question of what the differences are between the slow negative feedback mechanism based on SFA, see [35, 44–48], and the recently proposed positive feedback mechanism based on h-currents, see [21, 22] which have already been shown to induce SO-like dynamics. Simultaneous investigations of h-currents and SFA were already conducted. [49] used fluorescent dye in the dentate gyrus of rats and unmodified versus blocked HCN-channel<sup>2</sup> recordings to show that in the presence of HCN channels action potential (AP) initiation is enhanced during sustained firing and the propagation of AP patterns is sped up. They observe that in the presence of HCN channels, hyperpolarizing  $\text{Na}^+$ - $\text{K}^+$  currents are opposed. [50] included both HCN (h-current based adaptation) and M-channel (SFA) dynamics in a spiking neural network to investigate their role in seizure events in epilepsy patients. [22] found, in slice experiments, that blocking h-currents results in prolonged up- and down-state durations, effectively decreasing the temporal oscillation frequency. With their computational model they produce adaptation-driven SOs between up- and down-states where the implemented h-current and SFA based adaptation alternate in activation, depending on the membrane potential with h-currents active in

---

<sup>2</sup> HCN channels: Hyperpolarization-activated cyclic nucleotide gated channels correspond to h-current based adaptation.

down-, and inactive in up-states while the opposite is the case for SFA. With the model, they recreated the results found in vitro, prolonging up- and down-state durations, if the strength of h-currents is further reduced. [21] tested whether a spatial gradient in excitability, degree of recurrent excitation, or strength of the SFA current would induce a sequential activation of cortical neurons (i.e, up-state onset) along the dorso-ventral axis of the rat post-subiculum with a synchronous deactivation of the up-state. They observed this in vivo in naturally sleeping mice prior to their in-silico experiments. Neither gradient was able to replicate the experimentally observed dynamics. Including h-currents, on the other hand, with decreasing strength along the dorso-ventral axis replicated their results. A detailed analysis of the two opposing mechanisms shaping the spatio-temporal neural dynamics, however, has not yet been performed.

To address this, we implement a Wilson-Cowan field model and consider two nonlinear adaptation mechanisms, a negative feedback mechanism induced by high neural activity and a positive feedback mechanism induced by low neural activity, capturing the most prominent features of SFA- vs h-current based adaptation. The model is implemented on a one-dimensional spatial domain with periodic boundary conditions. Each location contains two interacting populations of excitatory and inhibitory neurons that are spatially coupled by a Gaussian synaptic connectivity kernel. The excitatory populations are locally equipped with either one of the two adaptation mechanisms. Since both mechanisms act in a functionally similar way, we describe them with the same dynamical equation and consider the inverse mode of action (negative vs. positive feedback and activation during high- vs. low-activity states) by changing the sign of the adaptation strength and the gain of the activation function. The model is parameterized to fulfill various criteria that have been shown to play a role in the formation of adaptation-driven slow waves, e.g., regimes of bistability (where stable up- and down-states coexist) in a cortical network for SOs during sleep [51] and anesthesia [52], or strong excitatory recurrence [53].

We first show that in our formulation both adaptation mechanisms are mathematically equivalent under a compensatory external input to the excitatory populations that depends on the adaptation strength. A state space analysis shows that strong enough adaptation is necessary to produce spatio-temporal activity patterns in this system that only generates homogeneous or sta-

tionary activity when adaptation is weak. The dynamical landscape exhibits parallels with the models studied in [34–37], but our analysis additionally displays regimes with states that undergo Turing bifurcations at the border of regimes exhibiting oscillatory activity or bistability. Moreover, we show that the model system experiences two types of bistability. Secondly, we conducted numerical simulations and show that in the two-population model, contrary to the purely excitatory model with synaptic depression of [42], the adaptation strength is a modulatory factor for the adaptation-driven slow waves. Over the considered slices of state space, we observe an increase of dominant temporal frequencies, spatial frequencies, and travel speed of spatio-temporal activity patterns, the stronger the adaptation strength becomes. Numerical results agree with the results of the mathematical analysis performed before.

Due to the dynamical equivalence, the state spaces for the positive and negative feedback mechanisms are equal but shifted along the external input parameter of the excitatory population proportional to the adaptation strength. This finding may serve as a guideline for what differences to expect in a given neurobiological setting (e.g., when analyzing the effects of spatial gradients of adaptation strength as in [21]). Furthermore, the Wilson-Cowan field model with adaptation can serve as a reference when considering the influence of the additional differences in the physiological properties of SFA- and h-currents-based adaptation mechanisms.

## II. THE SPATIALLY EXTENDED ADAPTIVE WILSON-COWAN MODEL

We use the original Wilson-Cowan continuum model of [38] with integro-differential equations, including a convolution over a spatial domain, to investigate adaptation-driven traveling waves of SO-like dynamics. We include a third differential equation for an adaptation mechanism and connect it to the excitatory population to describe the effects of either high-activity induced negative or low-activity induced positive feedback mechanisms. In the following we refer to them as spike-frequency ( $a$ ) or h-current ( $h$ ) mediated adaptation although the model is a simplification that focuses only on their most prominent biophysical features. The equations of the activities  $u_e$  and  $u_i$  of the excitatory and inhibitory population and for the adaptation variable  $m$  are given by

$$\begin{aligned}
 \tau_e \frac{\partial}{\partial t} u_e(x, t) &= -u_e(x, t) + F_e(w_{ee}w_e(x) * u_e(x, t) - w_{ei}w_i(x) * u_i(x, t) - bm(x, t) + I_e) \\
 \tau_i \frac{\partial}{\partial t} u_i(x, t) &= -u_i(x, t) + F_i(w_{ie}w_e(x) * u_e(x, t) - w_{ii}w_i(x) * u_i(x, t) + I_i) \\
 \tau_m \frac{\partial}{\partial t} m(x, t) &= -m(x, t) + F_m(u_e(x, t) - \mu),
 \end{aligned} \tag{1}$$

where the spatial convolution is defined as

$$w_j(x) * u_j(x, t) = \int_{-\infty}^{\infty} w_j(|x - y|) u_j(y, t) dy, \\ j \in \{e, i\}.$$

The spatial kernel is given by the normalized (i.e.,  $\int_{-\infty}^{\infty} w_j(x) dx = 1$ ) Gaussian

$$w_j(|x - y|) = \frac{1}{\sqrt{2\pi}\sigma_j} e^{-\frac{\|x-y\|^2}{2\sigma_j^2}}, \quad (2)$$

with width  $\sigma_j$ ,  $j \in \{e, i\}$ . The transfer functions are sigmoidal,

$$F_j(x) = \frac{1}{1 + e^{-\beta_j x}}, \quad j \in \{e, i, m\}. \quad (3)$$

The coupling strengths between the excitatory and inhibitory populations are given by connectivity weights  $w_{jl}$ ,  $j, l \in \{e, i\}$ , in Eq. (1). The membrane time constants are designated with  $\tau_j$ ,  $j \in \{e, i\}$ . The adaptation mechanisms  $m(x, t)$  are discussed in detail in Section II A; they are parametrized by a strength value  $b$ , a time constant  $\tau_m$ , and a gain parameter  $\beta_m$ . Due to the transfer function in Eq. (3) being a sigmoid between zero and one, we interpret the activity variables  $u_e$  and  $u_i$  as the proportion of neurons firing per unit time [54]. Its gain parameter is denoted by  $\beta_j$ . The kernel widths in Eq. (2) determine the extent to which populations are effectively connected in space. Kernel widths are chosen to be smaller for excitatory and broader for inhibitory interactions, effectively implementing a Mexican-hat shaped interaction between different locations. The parameters that are used in this study were adjusted such that adaptation-driven SOs are generated with an additional noisy external input (see [34, 46]), fast excitation-inhibition driven oscillations can emerge (see [55]), and the system with and without adaptation shows regimes of bistability since this has been shown to play a crucial part in the formation of SOs (see [51, 56]).

The model is implemented as a one-dimensional neural field with periodic boundary conditions and a homogeneous connectivity profile. To reduce the effects of the finite size on the dynamics, we combine a large ring of length  $L = 600$  with comparably small widths  $\sigma_j$ ,  $j \in \{e, i\}$ , of the spatial kernels. The ring is discretized into  $n$  positions, each of which is equipped with a node whose dynamics is described by Eqs. (1). Therefore, the integration space step is given by  $dx = \frac{L}{n}$ .

### A. The adaptation mechanisms

The excitatory populations are equipped with an adaptation mechanism, generally understood as a process (not restricted to the brain) that modulates the effect of a sustained input but acts on a slower time scale (see [57]). In the following, we distinguish two adaptation

TABLE I. List of model parameters. The abbreviations “exc” and “inh” stand for “excitatory population” and “inhibitory population”, respectively.

Parameter	Value	Description
$\mu_e$	0	Excitatory threshold
$\mu_i$	0	Inhibitory threshold
$\beta_e$	5	Excitatory gain
$\beta_i$	5	Inhibitory gain
$w_{ee}$	3.2	Coupling strength exc to exc
$w_{ei}$	2.6	Coupling strength inh to exc
$w_{ie}$	3.3	Coupling strength exc to inh
$w_{ii}$	0.9	Coupling strength inh to inh
$I_e$	[-2.5, 2]	External input current to exc
$I_i$	[-3.5, 1]	External input current to inh
$\tau_e$	10	Membrane time constant of exc
$\tau_i$	15	Membrane time constant of inh
$\sigma_e$	1	Spatial spread of exc
$\sigma_i$	3	Spatial spread of inh
$\mu$	0.4	Adaptation threshold
$dx$	0.3	Integration space step
$L$	600	Length (circumference) of ring
$b$	[0, 1]	SFA strength
$\tau_m$	300	SFA time constant
$\beta_m$	10	SFA gain
$-b$	[0, 1]	H-current strength
$\tau_m$	300	H-current time constant
$\beta_m$	-10	H-current gain

processes caused by different types of somatic conductances in cortical neurons (see [58]). Spike-frequency adaptation (SFA), a negative feedback mechanism, is mediated by slow potassium currents which activate when the activity of the excitatory population is high. This causes a hyperpolarizing feedback current which effectively inhibits the neural response of excitatory neurons (see [47]). H-current based adaptation is mediated by hyperpolarization-activated nucleotide-gated channels (see [59]) which open if the excitatory population is in a low-activity state and return positive feedback, i.e., effectively excite the excitatory population. Functionally, the adaptation mechanisms are similar (see [60] for SFA, for h-currents see [61] where the authors discuss h-currents in thalamic neurons, and see [21, 58] for both adaptation mechanisms in cortical neurons), so that we can describe their main effects by the same differential equation (last equation in Eqs. (1), see [21]) and include the inverse mode of action (positive versus negative feedback, activated during high- versus low-activity values) by changing the sign of the parameters for adaptation strength  $b$  and adaptation gain  $\beta_m$ . Parameters are summarized in Table I.

## B. Fixed points and stability analysis of the model with adaptation

To determine the fixed points we consider a single Wilson-Cowan node. Due to the normalization of the kernel, its fixed points are equivalent to the fixed points of the spatially extended model. Let  $\frac{\partial u_e}{\partial t} = \frac{\partial u_i}{\partial t} = 0$  in Eqs. (1). From  $\frac{\partial m}{\partial t} = 0$  we obtain  $m = F_m(u_e)$  which we insert in the equation for the excitatory population. The nullclines  $f(u_e)$  and  $g(u_i)$  are then given by

$$u_i = f(u_e) = \frac{1}{w_{ei}} (w_{ee}u_e + I_e - bF_j(u_e) - F_e^{-1}(u_e)),$$

$$j \in \{a, h\},$$

$$u_e = g(u_i) = \frac{1}{w_{ie}} (w_{ii}u_i - I_i + F_i^{-1}(u_i)).$$

A point  $(\tilde{u}_e, \tilde{u}_i, \tilde{m}) \in (0, 1)^3$  is a fixed point if  $f(\tilde{u}_e) = \tilde{u}_i$ ,  $g(\tilde{u}_i) = \tilde{u}_e$ , and  $F_m(\tilde{u}_e) = \tilde{m}^3$ .

We apply the procedure from Harris & Ermentrout [31], Byrne et al [62], and Wyller et al [32]<sup>4</sup> to investigate the stability of the homogeneous steady states (i.e., the fixed points) of field models. To do so, we add a small spatial perturbation to the homogeneous steady state,

$$\begin{aligned} u_e(x, t) &= \tilde{u}_e + \chi(x, t) \\ u_i(x, t) &= \tilde{u}_i + \varphi(x, t) \\ m(x, t) &= \tilde{m} + \phi(x, t). \end{aligned} \quad (4)$$

Then, we insert Eqs. (4) into Eqs. (1) and linearize the system around the homogeneous steady state by applying a Taylor expansion up to the first order in  $\chi(x, t)$ ,  $\varphi(x, t)$ , and  $\phi(x, t)$ . We obtain

$$\begin{aligned} \tau_e \partial_t \chi &= -\chi + w_{ee} F'_e(B_e) w_e * \chi - w_{ei} F'_e(B_e) w_i * \varphi - b F'_e(B_e) \phi \\ \tau_i \partial_t \varphi &= -\varphi + w_{ie} F'_i(B_i) w_e * \chi - w_{ii} F'_i(B_i) w_i * \varphi \\ \tau_m \partial_t \phi &= -\phi + F'_m(\tilde{u}_e) \chi, \end{aligned}$$

where  $B_l = w_{le} \tilde{u}_e - w_{li} \tilde{u}_i + I_l$ ,  $l \in \{e, i\}$ . The zero order terms vanish for  $\tilde{u}_e$  and  $\tilde{u}_i$ , because the spatial kernels are normalized to one. To transform this set of IDEs into a set of ordinary differential equations (ODEs), we

exploit the fact that a convolution in the spatial domain is a product in the frequency domain (i.e.,  $w(x) * \chi(x, t) = \hat{w}(k) \hat{\chi}(k, t)$ , where  $\hat{\cdot}$  denotes the Fourier Transformation). This leads to the ODE system

$$\begin{aligned} \tau_e \partial_t \hat{\chi} &= -\hat{\chi} + w_{ee} F'_e(B_e) \hat{w}_e \hat{\chi} - w_{ei} F'_e(B_e) \hat{w}_i \hat{\varphi} - b F'_e(B_e) \hat{\phi} \\ \tau_i \partial_t \hat{\varphi} &= -\hat{\varphi} + w_{ie} F'_i(B_i) \hat{w}_e \hat{\chi} - w_{ii} F'_i(B_i) \hat{w}_i \hat{\varphi} \\ \tau_m \partial_t \hat{\phi} &= -\hat{\phi} + F'_m(\tilde{u}_e) \hat{\chi}. \end{aligned} \quad (5)$$

For  $\vec{X} = \begin{pmatrix} \hat{\chi} \\ \hat{\varphi} \\ \hat{\phi} \end{pmatrix}$ , Eqs. (5) can be written in vector nota-

tion,  $\partial_t \vec{X} = A_3(k) \vec{X}$ , where

$$A_3(k) = \begin{bmatrix} -\frac{1}{\tau_e} + \frac{w_{ee}}{\tau_e} F'_e(B_e) \hat{w}_e(k) & -\frac{w_{ei}}{\tau_e} F'_e(B_e) \hat{w}_i(k) & -\frac{b}{\tau_e} F'_e(B_e) \\ \frac{w_{ie}}{\tau_i} F'_i(B_i) \hat{w}_e(k) & -\frac{1}{\tau_i} - \frac{w_{ii}}{\tau_i} F'_i(B_i) \hat{w}_i(k) & 0 \\ \frac{F'_m(\tilde{u}_e)}{\tau_m} & 0 & -\frac{1}{\tau_m} \end{bmatrix} =: \begin{bmatrix} a_{11}(k) & a_{12}(k) & a_{13} \\ a_{21}(k) & a_{22}(k) & a_{23} \\ a_{31} & a_{32} & a_{33} \end{bmatrix}, \quad (6)$$

<sup>3</sup> The stability analysis of the system without adaptation, i.e.,  $b = 0$ , is covered in Appendix A 1.

<sup>4</sup> [32], however, assumes that the fixed point values  $\tilde{u}_e$  and  $\tilde{u}_i$  are equal.

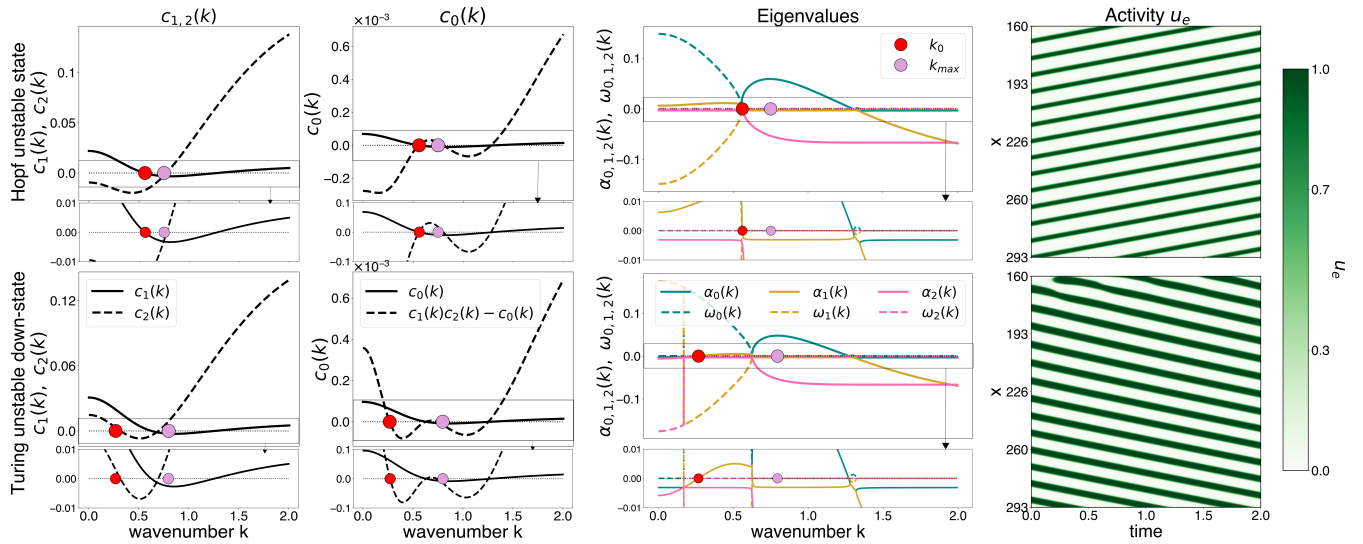


FIG. 1. Examples for static (top row) and dynamic (bottom row) Turing bifurcations in a Hopf- (top row) and Turing-unstable state (bottom row) for the system with h-currents. Panels from left to right show (cf. Eqs. (7)): Coefficients  $c_1(k)$  (solid line) and  $c_2(k)$  (dashed line), coefficient  $c_0(k)$  (solid line) and condition  $c_1(k)c_2(k) - c_0(k)$  (dashed line), real ( $\alpha_{0,1,2}(k)$ , solid lines) and imaginary ( $\omega_{0,1,2}(k)$ , dashed lines) parts of the eigenvalues of the linearization matrix, and the corresponding activity pattern  $u_e(x, t)$ . Circles denote the wavenumbers  $k_0$  (red) and  $k_{max}$  (pink) (see text). Insets below each plot show close-ups of the thin boxes. Values for the external input currents and the adaptation parameter were  $(I_e, I_i) = (-0.7, -0.6)$ ,  $b = -0.5$  (top row) and  $(I_e, I_i) = (-0.3, -0.3)$ ,  $b = -0.5$  (bottom row). All other parameters are given in Table I.

$B_e := w_{ee}\tilde{u}_e - w_{ei}\tilde{u}_i - bF_m(\tilde{u}_e) + I_e$  and  $B_i := w_{ie}\tilde{u}_e - w_{ii}\tilde{u}_i + I_i$ . The stability of the fixed point can be char-

acterized by the eigenvalues  $\lambda_j(k) = \alpha_j(k) + i\omega_j(k)$ ,  $j \in \{0, 1, 2\}$ , of the linearization matrix (Jacobian)  $A_3(k)$ , where  $i$  denotes the imaginary unit. The eigenvalues correspond to the roots of the cubic polynomial

$$\begin{aligned} \det(A_3(k) - \lambda \mathbf{I}) &= \lambda^3 + \lambda^2(-(a_{11}(k) + a_{22}(k) + a_{33})) \\ &\quad + \lambda(a_{11}(k)a_{22}(k) + a_{11}(k)a_{33} + a_{22}(k)a_{33} - a_{13}a_{31} - a_{12}(k)a_{21}(k)) \\ &\quad + (-a_{11}(k)a_{22}(k)a_{33} + a_{22}(k)a_{13}a_{31} + a_{33}a_{12}(k)a_{21}(k)) \\ &= \lambda^3 + \lambda^2 c_2(k) + \lambda c_1(k) + c_0(k) \end{aligned}$$

with

$$\begin{aligned} c_0(k) &= -a_{11}(k)a_{22}(k)a_{33} + a_{22}(k)a_{13}a_{31} \\ &\quad + a_{33}a_{12}(k)a_{21}(k) \\ c_1(k) &= a_{11}(k)a_{22}(k) + a_{11}(k)a_{33} + a_{22}(k)a_{33} \\ &\quad - a_{13}a_{31} - a_{12}(k)a_{21}(k) \\ c_2(k) &= -(a_{11}(k) + a_{22}(k) + a_{33}). \end{aligned} \quad (7)$$

Fixed points with  $\alpha_j(k) < 0$  for all  $j \in \{0, 1, 2\}$  are stable. If the model system has a fixed point which is unstable at  $k = 0$  (i.e.,  $\alpha_j(0) \geq 0$  for at least one  $j \in \{0, 1, 2\}$ , see Fig. 1, first row), we call the state of the system *Hopf-unstable*, if  $\omega_j(0) \neq 0$ , or simply *unstable*, if  $\omega_j(0) = 0$ .

A fixed point  $(\tilde{u}_e, \tilde{u}_i, \tilde{m})$  undergoes a static Turing bifurcation at  $k_0 > 0$  if  $c_0(k_0) = 0$ , i.e., if one of the

eigenvalues is zero for this wavenumber. This is illustrated in Fig. 1, first row, where the condition is met for the wavenumber  $k_0$  indicated by the red circle. If  $c_2(k_0)c_1(k_0) - c_0(k_0) = 0$  for  $c_1(k_0) > 0$ , i.e., if one eigenvalue at this wavenumber is purely imaginary, the fixed point undergoes a dynamic Turing bifurcation (also called a Turing-Hopf bifurcation, see [32, 43, 62]). This is illustrated in Fig. 1, second row, where the condition is met, for example, for the wavenumber indicated by the red marker. We refer to a fixed point that is stable at  $k = 0$  but undergoes a static or a dynamic Turing bifurcation for a  $k_0 > 0$  under the umbrella term “*Turing-unstable*”. For the investigated parameterizations, Hopf-unstable states always undergo a Turing bifurcation for some  $k_0 > 0$  (see, e.g., Fig. 1, first row).

TABLE II. Summary of the bifurcations and instabilities that occur in the model system for the investigated parameter settings. Row "Name" lists the names by which the states are referred to in this study, row "Prerequisites" contains the conditions that must be met at the bifurcation, and row "Patterns" enumerates the corresponding type of activity pattern emerging in a state undergoing the named bifurcation.

Bifurcation	Hopf-bifurcation	Static Turing-bifurcation	Dynamic Turing-bifurcation
Name	Hopf-unstable state	Turing-unstable down-/up-state (in bi), if stable at $k = 0$ , or Hopf-unstable state, if unstable at $k = 0$ with non-zero imaginary part <sup>a</sup>	Turing-unstable down-/up-state (in bi), if stable at $k = 0$ , or Hopf-unstable state, if unstable at $k = 0$ with non-zero imaginary part <sup>a</sup>
Prerequisites	$\alpha_j(0) \geq 0$ , and $\omega_j(0) \neq 0$ for at least one $j \in \{0, 1, 2\}$	$c_0(k_0) = 0$ for $k_0 > 0$ (i.e. there is at least one eigenvalue with $\alpha_j(k_0) = \omega_j(k_0) = 0$ )	$c_2(k_0)c_1(k_0) - c_0(k_0) = 0$ for $c_j(k_0) > 0$ , $j \in \{0, 1, 2\}$ , and $k_0 > 0$ (i.e. there is at least one eigenvalue with $\alpha_j(k_0) = 0, \omega_j(k_0) \neq 0$ )
Patterns	Purely temporal oscillations	Purely spatial oscillations	Spatio-temporal activity patterns

<sup>a</sup> Note that for all investigated parameterizations, Hopf-unstable states also undergo a Turing bifurcation. Henceforth, we summarize fixed points that are unstable at  $k = 0$  with non-zero imaginary part under the umbrella term "*Hopf-unstable*"

Since we are particularly interested in adaptation-driven slow alternations between high- (up) and low-activity (down) states, we distinguish up- ( $\tilde{u}_e \geq 0.4$ ) from down- ( $\tilde{u}_e < 0.4$ ) states by the fixed point value of the excitatory population. Consequently, when a Turing bifurcation emerges in an up- (down-) state, we call the state *Turing-unstable up- (down-) state*. In addition, the model exhibits regimes of bistability where stable up- and down-states coexist for the same location in state space. If either one of the two states loses stability for some  $k_0 > 0$  due to an emerging Turing bifurcation while the coexisting fixed point remains stable, we call the Turing-unstable state a *Turing unstable up- or down-state in bi*, respectively. Table II summarizes all types of bifurcations that emerge in the model for the investigated parameter settings and how we refer to them throughout this study.

Note that there is a difference in the instability of modes between Hopf-unstable states undergoing a Turing bifurcation and other Turing-unstable states which is exemplified in Fig. 1, third column (Eigenvalues). In Hopf-unstable states, unstable modes already occur for wavenumber values  $0 \leq k \leq k_0$ , while in other Turing-unstable states the minimum wavenumber for unstable

modes is  $k_0$ .

### C. Wavenumbers

If a fixed point is identified as Turing- or Hopf-unstable, we compute the smallest wavenumber  $k_0 > 0$  at which one of the conditions listed in Table II is met. Examples are shown in Fig. 1, where  $k_0$  is marked by the red circles. Additionally, we determine the wavenumber  $k_{max}$  (see pink circles in Fig. 1) for which the corresponding unstable mode grows most rapidly, i.e., for which the real part  $\alpha_j(k)$  of the largest eigenvalue becomes maximal,  $k_{max} = \text{argmax}_k(\max_j \alpha_j(k))$ . Wavenumbers were computed, because they determine the wavelengths of the spatio-temporal patterns that emerge in a fixed point that undergoes one of the aforementioned bifurcations (see [23, 43, 63]).

### D. Symmetries and equivalence of mechanisms

Let Eqs. (1),

$$S(u_e, u_i, m) = \begin{pmatrix} \tau_e \frac{\partial u_e}{\partial t} \\ \tau_i \frac{\partial u_i}{\partial t} \\ \tau_m \frac{\partial m}{\partial t} \end{pmatrix} = \begin{pmatrix} -u_e(x, t) + F_e(w_{ee}w_e(x) * u_e(x, t) - w_{ei}w_i(x) * u_i(x, t) - bm(x, t) + I_e) \\ -u_i(x, t) + F_i(w_{ie}w_e(x) * u_e(x, t) - w_{ii}w_i(x) * u_i(x, t) + I_i) \\ -m(x, t) + F_m(u_e(x, t) - \mu) \end{pmatrix}, \quad (8)$$

be the system with SFA (i.e., let  $b, \beta_m > 0$ ), and let  $T : [0, 1]^3 \rightarrow [0, 1]^3$  with

$$T : (u_e, u_i, m)^\top \mapsto (u_e, u_i, 1 - m)^\top$$

be an isomorphic transformation. Then we have  $\frac{\partial}{\partial t} [T((u_e(x, t), u_i(x, t), m(x, t))^\top)] = \begin{pmatrix} \frac{\partial u_e}{\partial t} \\ \frac{\partial u_i}{\partial t} \\ -\frac{\partial m}{\partial t} \end{pmatrix}^\top$ . Inserting the transformation into Eqs. (8) we obtain

$$\begin{aligned}
S(\mathbf{T}(\mathbf{u}_e, \mathbf{u}_i, \mathbf{m})) &= \begin{pmatrix} \tau_e \frac{\partial u_e}{\partial t} \\ \tau_i \frac{\partial u_i}{\partial t} \\ -\tau_m \frac{\partial m}{\partial t} \end{pmatrix} = \begin{pmatrix} -u_e(x, t) + F_e(w_{ee}w_e(x) * u_e(x, t) - w_{ei}w_i(x) * u_i(x, t) - \mathbf{b}(1 - \mathbf{m}(\mathbf{x}, \mathbf{t})) + I_e) \\ -u_i(x, t) + F_i(w_{ie}w_e(x) * u_e(x, t) - w_{ii}w_i(x) * u_i(x, t) + I_i) \\ -(-(\mathbf{1} - \mathbf{m}(\mathbf{x}, \mathbf{t})) + \underbrace{F_m(u_e(x, t) - \mu)}_{=1 - F_m(\mu - u_e)}) \end{pmatrix} \\
&= \begin{pmatrix} -u_e(x, t) + F_e(w_{ee}w_e(x) * u_e(x, t) - w_{ei}w_i(x) * u_i(x, t) + bm(x, t) - b + I_e) \\ -u_i(x, t) + F_i(w_{ie}w_e(x) * u_e(x, t) - w_{ii}w_i(x) * u_i(x, t) + I_i) \\ -m(x, t) + F_m(\mu - u_e(x, t)) \end{pmatrix}.
\end{aligned}$$

This system of equations is, given the choice of  $F_m$  (Eq. (3)), equivalent to the system of Eqs. (1) for h-currents if  $-b \leftarrow b$  and  $-\beta_m \leftarrow \beta_m$  (see Table I) and the external input to the excitatory population in the system with SFA is decreased by the value of  $b$ , i.e.,  $I_e^h = I_e^a - b$ . The superscripts  $^a, ^h$  indicate the difference between the variables and parameters for SFA and h-currents, respectively. Hence, both adaptation mechanisms are dynamically equivalent under the transformation  $T$ , if  $I_e$  is correspondingly changed and if  $F_m^a(x) = 1 - F_m^h(x)$  holds for the adaptation nonlinearity. This equivalence also tells us that a fixed point  $(\tilde{u}_e^a, \tilde{u}_i^a, \tilde{m}^a)$  for the system

with SFA corresponds to a fixed point  $(\tilde{u}_e^h, \tilde{u}_i^h, 1 - \tilde{m}^h)$  for the system with h-currents and that the dynamical landscape for h-currents should be the same as the dynamical landscape for SFA, but shifted along the  $I_e$ -axis by the value  $b$ .

Beyond dynamical equivalence between the adaptation mechanisms, we also have a symmetry for each system within itself. Let  $T : [0, 1]^3 \rightarrow [0, 1]^3$  with  $T : (u_e, u_i, m)^\top \mapsto (1 - u_e, 1 - u_i, 1 - m)^\top$  be another isomorphic transformation such that  $\frac{\partial}{\partial t} [T((u_e(x, t), u_i(x, t), m(x, t))^\top)] = (-\frac{\partial u_e}{\partial t}, -\frac{\partial u_i}{\partial t}, -\frac{\partial m}{\partial t})^\top$ . Inserting this in Eqs. (8) we obtain

$$\begin{aligned}
\begin{pmatrix} -\tau_e \frac{\partial u_e}{\partial t} \\ -\tau_i \frac{\partial u_i}{\partial t} \\ -\tau_m \frac{\partial m}{\partial t} \end{pmatrix} &= \begin{pmatrix} 1 - u_e(x, t) - F_e(w_{ee}w_e(x) * (1 - u_e(x, t)) - w_{ei}w_i(x) * (1 - u_i(x, t)) - b(1 - m(x, t)) + I_e) \\ 1 - u_i(x, t) - F_i(w_{ie}w_e(x) * (1 - u_e(x, t)) - w_{ii}w_i(x) * (1 - u_i(x, t)) + I_i) \\ 1 - m(x, t) - F_m((1 - u_e(x, t)) - \mu) \end{pmatrix} \\
&= \begin{pmatrix} -u_e(x, t) + F_e(w_{ee}w_e(x) * u_e(x, t) - w_{ei}w_i(x) * u_i(x, t) - bm(x, t) - I_e - w_{ee} + w_{ei} + b) \\ -u_i(x, t) + F_i(w_{ie}w_e(x) * u_e(x, t) - w_{ii}w_i(x) * u_i(x, t) - I_i - w_{ie} + w_{ii}) \\ -m(x, t) + F_m(u_e(x, t) + \mu - 1) \end{pmatrix}. \quad (9)
\end{aligned}$$

If  $\hat{I}_e = -I_e + b - w_{ee} + w_{ei}$ ,  $\hat{I}_i = -I_i - w_{ie} + w_{ii}$ , and  $\hat{\mu} = 1 - \mu$ , then the system (9) is equivalent to Eqs. (1) for both SFA and h-currents. This induces an approximate point symmetry of state space at  $(I_e^c, I_i^c) = (\frac{b - w_{ee} + w_{ei}}{2}, \frac{-w_{ie} + w_{ii}}{2})$  between  $(u_e, u_i, m)$  and  $(1 - u_e, 1 - u_i, 1 - m)$  which becomes exact for  $\mu = 0.5$ . Since  $\mu = 0.4$  in this study, an exact symmetry is only achieved for  $b = 0$  (Fig. 2A, first column, where the black dot in the middle of the orange regime denotes the center of the point reflection).

### III. OVERVIEW OF STATE SPACE AND ITS CHANGES WITH ADAPTATION STRENGTH

Figure 2 shows the results of the analytical investigation for the system with h-currents with increasing adaptation strength (Fig. 2A) and examples for the emerging spatio-temporal patterns (Fig. 2B) for all regimes of Hopf

or Turing instability. Without adaptation ( $b = 0$ ), we observe a Hopf-unstable regime (orange) in which both temporal (similar to Fig. 2B, panel 3(\*), for  $b = -0.5$ ) and spatial (see Fig. 2B, panel 1) patterns emerge. With adaptation, the Hopf regime is also apparent but the activity patterns can be either temporal (Fig. 2B, panel 3(\*)) or spatio-temporal (Fig. 2B, panel 3). Close to the bifurcation lines of the Hopf-unstable regime, we observe the emergence of Turing instability in down-states (upper border; for an activity example see Fig. 2B, panel 4) and in up-states (lower border; for activity example see Fig. 2B, panel 6). Beyond the Turing instability in down-(up-) states, to the left (right) side of the state spaces in Fig. 2A, there exists a regime, marked dark blue (dark red), where a single down- (up-) state fixed point is stable. We also see regimes of three fixed points including one stable up-state (dark beige) while the other two fixed points are unstable and vice versa with one stable down-state (light beige). Activity traces in these regimes are

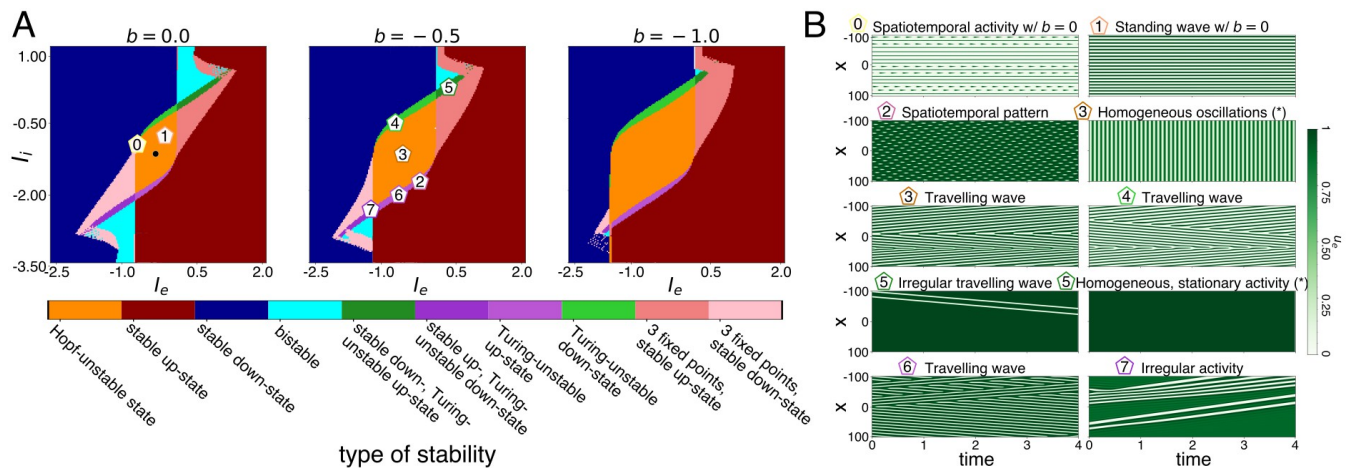


FIG. 2. State spaces and activity patterns for the Wilson-Cowan model with h-currents. **A** Results of the stability analyses for a slice of parameter space spanned by the external input currents  $(I_e, I_i) \in [-2.5, 2] \times [-3.5, 1]$  for increasing adaptation strength  $|b| \in \{0, 0.5, 1.0\}$  (left to right). Colors denote the different dynamical regimes (see legend). Pentagon markers identify the positions in state space corresponding to the activity traces shown in **B**. Resolution of state space is  $181 \times 181$ . The black dot in the state space for  $b = 0$  denotes center of point symmetry (see Section IID). **B** Activity traces  $u_e(x, t)$  for different locations in state space (see Table III in Appendix B 5), denoted by pentagons in **A**. Two types of bistability are exemplified in panels 3, 3(\*) and 5, 5(\*) (see text). Lighter green denotes low, darker green high activity values (see color bar). All simulations were initialized around their corresponding fixed points, except for the activity traces marked with (\*) which were initialized close to zero (see Appendix B 1).

similar to the activities shown in Fig. 2B, panels 5(\*) and 7. Initializations close to zero always converge to the existing stable fixed point while initializations around the unstable states cause irregular traveling waves. Further, to both corner ends (upper right and lower left), we find a regime of bistability between up- and down-states (light blue) next to bistable regimes, where a stable down-state coexists with a Turing instability in the up-state (dark purple) and vice versa (dark green). Figure 2C, panel 5, shows that the activity converges to the activity caused by the Turing bifurcation in the down-state, if initialized close to the Turing-unstable down-state. Initialized close to zero, the activity converges to the stable up-state (see activity 5(\*)). The pattern emerging in the Turing-unstable down-state of panel 5 shows down-state waves traveling over an otherwise stable up-state activity, unlike the traveling waves shown in panels 4 and 6, where no other stable fixed point coexists. Furthermore, in some states, the activity patterns can become irregular (see Fig. 2B, panel 7), such that they do not converge to a periodic, equidistant, or otherwise regular pattern. Such irregular patterns predominantly occur at the border of different regimes or in states where another attractor, e.g., a stable fixed point, coexists.

The Hopf-unstable states further undergo Turing bifurcations beyond the Hopf bifurcation at  $k = 0$  (see, for example, Fig. 1, top row, third panel), giving rise to spatial (for  $b = 0$ , static Turing bifurcations) or spatio-temporal (for  $b \neq 0$ , dynamic Turing bifurcations) patterns. Initialized close to zero, states in the Hopf regime converge to fast, spatially homogeneous, temporal oscillations caused by the Hopf instability, while initializations

close to the fixed points converge to spatial or spatio-temporal patterns. In this regime, the system thus experiences a second type of bistability that is not caused by the coexistence of multiple fixed points<sup>5</sup>. However, there are two small areas in the Hopf-unstable regime for  $b = 0$  where exceptions occur and where spatio-temporal patterns are present (Fig. 2B, panel 0). These areas are located in the top left of the Hopf regime where a stable down-state, three fixed points with a stable down-state, a Hopf instability, and a Turing instability are getting close in parameter space, and in the bottom right corner, where the regimes of a stable up-state, a Hopf instability, three fixed points with a stable up-state, and a Turing instability meet. In these states, depending on the initialization, most of the ring converges toward the standing wave interspersed by a few traveling bumps (see Fig. 2B, panel 0). When adaptation strength increases, the bistable regime (light blue) shrinks and vanishes for values  $|b| > 1$ . The size of the Hopf-unstable regime (orange) and of the regime of three fixed points with a stable up-state (beige) increase, while the regime of three fixed points with a stable down-state decreases in size (light beige).

Figure 3 shows a comparison between the state spaces and activity traces for the systems with SFA and h-currents. We see in Fig. 3A that the dynamical regimes

<sup>5</sup> Note, however, that in the following the name “bistable regime” will refer to the light blue area in state space, where two stable fixed points coexist.

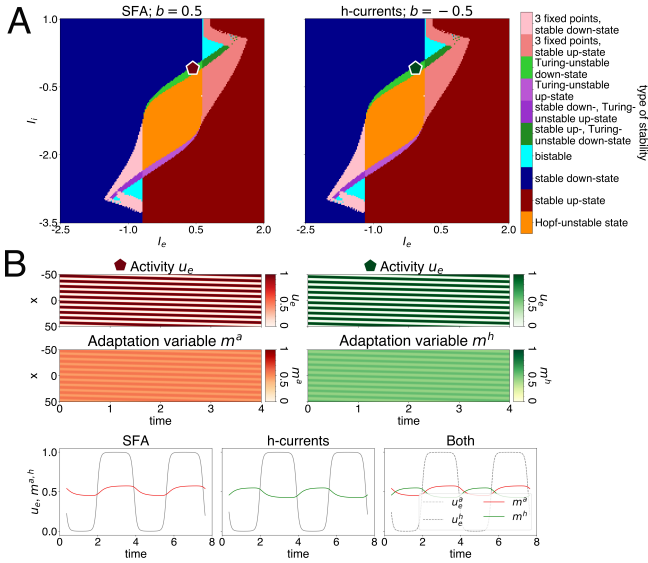


FIG. 3. Comparison of state spaces and activity patterns for both adaptation mechanisms. **A** Slices of state space for SFA (left) and h-currents (right) for  $|b| = 0.5$  spanned by the external input currents  $I_e$  and  $I_i$ . Colors denote the different dynamical regimes (see legend). Colored pentagon markers identify the positions in state space corresponding to the activity traces shown in B. The external input currents are  $(I_e, I_i) = (0.4, -0.3)$  for SFA and  $(I_e, I_i) = (-0.1, -0.3)$  for h-currents. **B** Top row: Activity traces  $u_e(x, t)$  for the locations in state space, marked in A. Middle row: Corresponding traces of the adaptation variable  $m$ . Bottom row: Activity traces and traces of the corresponding adaptation variable for a fixed spatial location for the traveling waves shown above for SFA (left panel) and h-currents (middle panel). All traces are superimposed in the right panel.

are equivalent for SFA (left) and h-currents (right), except for the shift to the right (left) by the absolute value  $|b|$  for SFA (h-currents), consistent with the required compensation of external inputs to the excitatory population (see Section IID). The rightward shift of the dynamical regimes for SFA compared to h-currents implies that the system requires more external input to the excitatory population to produce activity patterns beyond the spatially and temporally homogeneous steady states. We also see that equivalent positions (considering the required compensatory inputs) cause activity patterns to be equivalent under the transformation  $T$ , i.e., for  $m \leftarrow 1 - m$ , as exemplified in Fig. 3B.

For the investigated parameterization (see Table I), adaptation is required to cause the purely temporal or spatial patterns observed at  $b = 0$  to travel. We exemplify this in Fig. 4 where we show the real ( $\alpha_j(k)$ ) and imaginary ( $\omega_j(k)$ ) parts of all three eigenvalues  $\lambda_j(k) = \alpha_j(k) \pm i\omega_j(k)$  of the Jacobian (Eq. (6)) for a Hopf-unstable (upper row) and a Turing-unstable (center and bottom row) state. In the upper two rows, for small values of  $b$ , the zero crossings of the real parts of any eigenvalue coincide with non-zero imaginary parts,

resulting in a dynamic Turing bifurcation and enabling spatio-temporal patterns in that very state. For  $b = 0$  the imaginary part vanishes, resulting in a static Turing bifurcation. However, adaptation can not be arbitrarily weak and must be stronger than some threshold to show dynamic Turing bifurcations. In the bottom row of Fig. 4, for example, the Turing bifurcations are static for  $b = -0.02$  and  $b = -0.01$  and allow the system to produce standing waves for the corresponding activity traces (see Appendix A 3, Fig. 8). While the Turing bifurcation becomes dynamic for  $b = -0.03$ , all eigenvalues have negative real parts for  $b = -0.02$  for every  $k$  for which the imaginary part is non-zero, i.e., the system is stable whenever there is at least one eigenvalue  $j \in \{0, 1, 2\}$  such that  $\omega_j(k) \neq 0$ .

Additionally, we see in Fig. 4, as  $|b|$  increases, the imaginary part becomes larger which indicates faster temporal oscillations, since each mode is given by

$$\begin{aligned} \exp(\lambda(k)t) \exp(ikx) &= \exp(\underbrace{(\alpha(k) \pm i\omega(k))}_{=0}) \exp(ikx) \\ &= \exp(\underbrace{\pm i\omega(k)t}_{\omega \uparrow \text{ for } |b| \uparrow}) \exp(ikx). \end{aligned}$$

Above conclusions are confirmed for the entire slices of state space in Appendix A 1, Fig. 7, where we distinguish both types of bifurcations that occur.

#### IV. CHARACTERIZATION OF REGULAR SPATIO-TEMPORAL PATTERNS IN HOPF- AND TURING-UNSTABLE STATES

Figure 5 shows the results of the numerical investigation for the system with h-currents with increasing adaptation strength for the regimes of Hopf or Turing instability, where regular patterns occur. We did not consider the regimes of three fixed points (corresponding to dark and light beige in Fig. 2A), because numerical simulations close to the fixed points undergoing a Turing bifurcation lead to irregular propagation of activity fronts similar to the pattern exemplified in Fig. 2B, panel 7, which shows irregular activity emerging in a Turing-unstable up-state in bi.

Figure 5A shows the wavenumber  $k_{max}$  (top row), and the spatial,  $f_x$  (center row) and temporal frequencies,  $f_t$  (bottom row) of the emerging patterns for different locations in state space and for increasing adaptation strength.  $k_{max}$  values vary continuously across state space. Values are larger than 0.44 with highest values occurring in Turing-unstable states (see color bar). The spatial frequency,  $f_x$ , of the wave patterns change smoothly across state space for  $b = 0$  with the highest values occurring toward the center of the Hopf regime. Values decrease toward the borders. For  $b = -0.5$  and  $b = -1$ , the distribution of  $f_x$  becomes less smooth with non-equidistant, irregular patterns ( $r > 10^{-2}$ ) emerging toward the borders of the Hopf regime, where the regimes

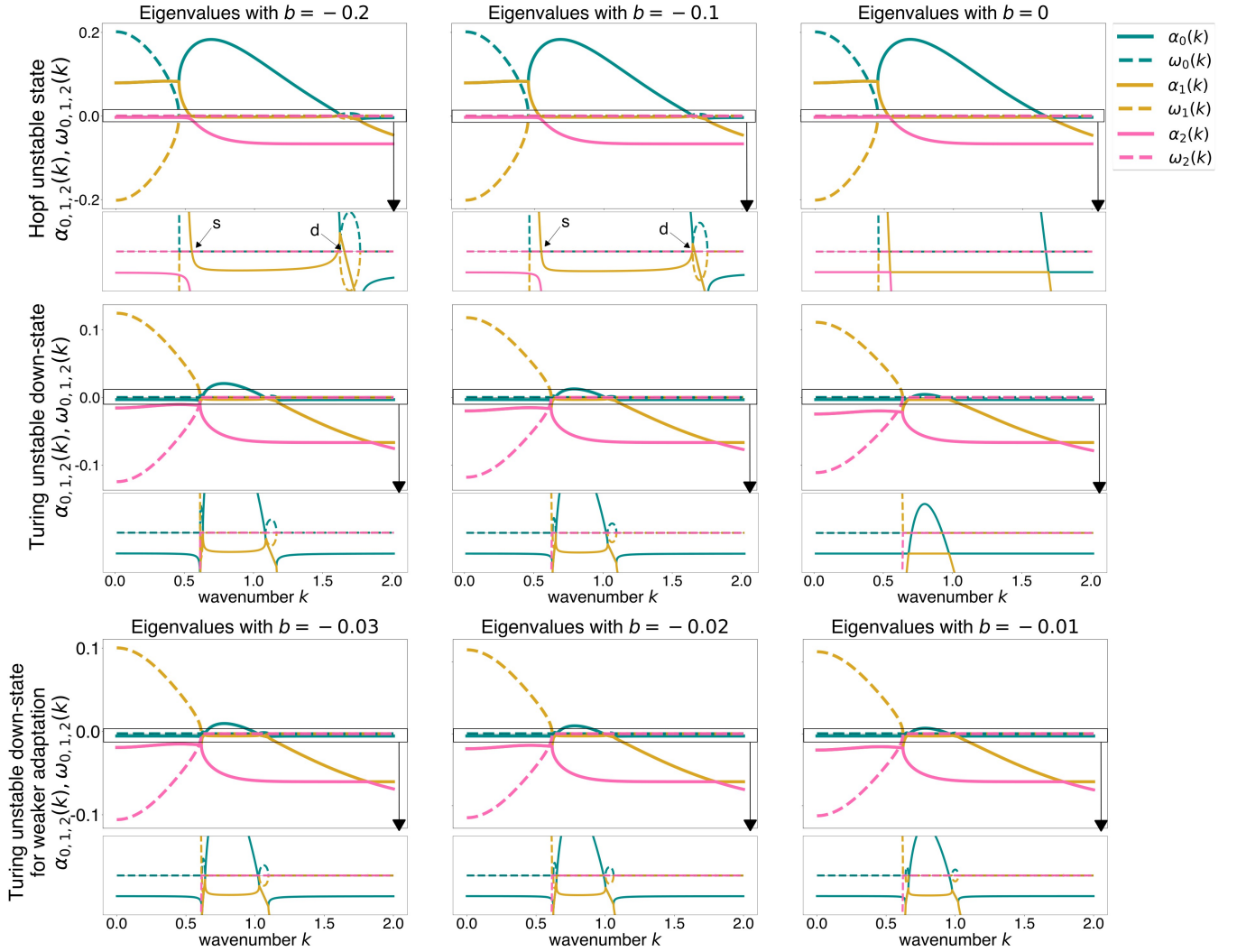


FIG. 4. Eigenvalue spectrum for small values of  $|b|$ . The panels show the real,  $\alpha_{0,1,2}(k)$ , (solid lines) and imaginary parts,  $\omega_{0,1,2}(k)$ , (dashed lines) of the eigenvalues of the linearization matrix in Eq. (6). Top row: Hopf-unstable state at  $(I_e, I_i) = (-0.35, -1.225)$ . Center row: Turing-unstable down-state at  $(I_e, I_i) = (-0.35, -0.55)$ . Bottom row: same Turing-unstable down-state as in the center row but with weaker adaptation. Adaptation strength  $|b|$  decreases from left to right. Lower panels show close-ups around the zero crossing of the real parts. The imaginary parts vanish for  $b = 0$ . Arrows in panels below the first two plots of the upper row indicate zero crossing of a static ( $s$ ) and dynamic ( $d$ ) Turing bifurcation.

of Turing instability, one stable fixed point, Hopf instability, and three fixed points with only one stable state meet (green areas inside instability regimes, Fig. 5A). The numerical simulations also confirm that the activity traces for  $b = 0$  are stationary spatial waves, as  $f_t$  is zero. For adaptation strong enough, waves start moving resulting in a finite value of  $f_t$  which increases with the value of  $|b|$  (see also Fig. 5B) confirming what is expected from the mathematical analysis. For increasing  $|b|$ , the averages of the wavenumbers  $k_0$ , and  $k_{max}$  increase in value, albeit the variance over state space is high.  $f_x$  increases with  $|b|$  consistent with the increase of the wavenumbers  $k_0$  and  $k_{max}$ . Additionally, the average temporal frequency increases steeply, which is expected from the increasing imaginary parts at the zero crossings of the real parts of

the eigenvalues as discussed in Section III. In Fig. 5C we compare the spatial frequencies of the simulated activity patterns (top row) with the expected spatial frequencies corresponding to the two wavenumbers  $k_0$ , i.e.,  $\frac{L \cdot k_0}{2\pi}$  (middle row), and  $k_{max}$ , i.e.,  $\frac{L \cdot k_{max}}{2\pi}$  (bottom row). Since  $k_{max}$  identifies the most rapidly growing unstable mode, expectations are to have highest similarity of spatial frequencies and frequencies corresponding to  $k_{max}$ . The distribution of spatial frequencies across Hopf states roughly agrees with this hypothesis (The Wasserstein distance between the distributions of  $f_x$  and  $\frac{L \cdot k_{max}}{2\pi}$  is 3.2 and 12.9 between the distributions of  $f_x$  and  $\frac{L \cdot k_0}{2\pi}$ ), the spatial frequencies observed in Turing-unstable down- and up-states, however, agree better with  $k_0$  (The Wasserstein distance between the distributions of  $f_x$  and  $\frac{L \cdot k_{max}}{2\pi}$  are

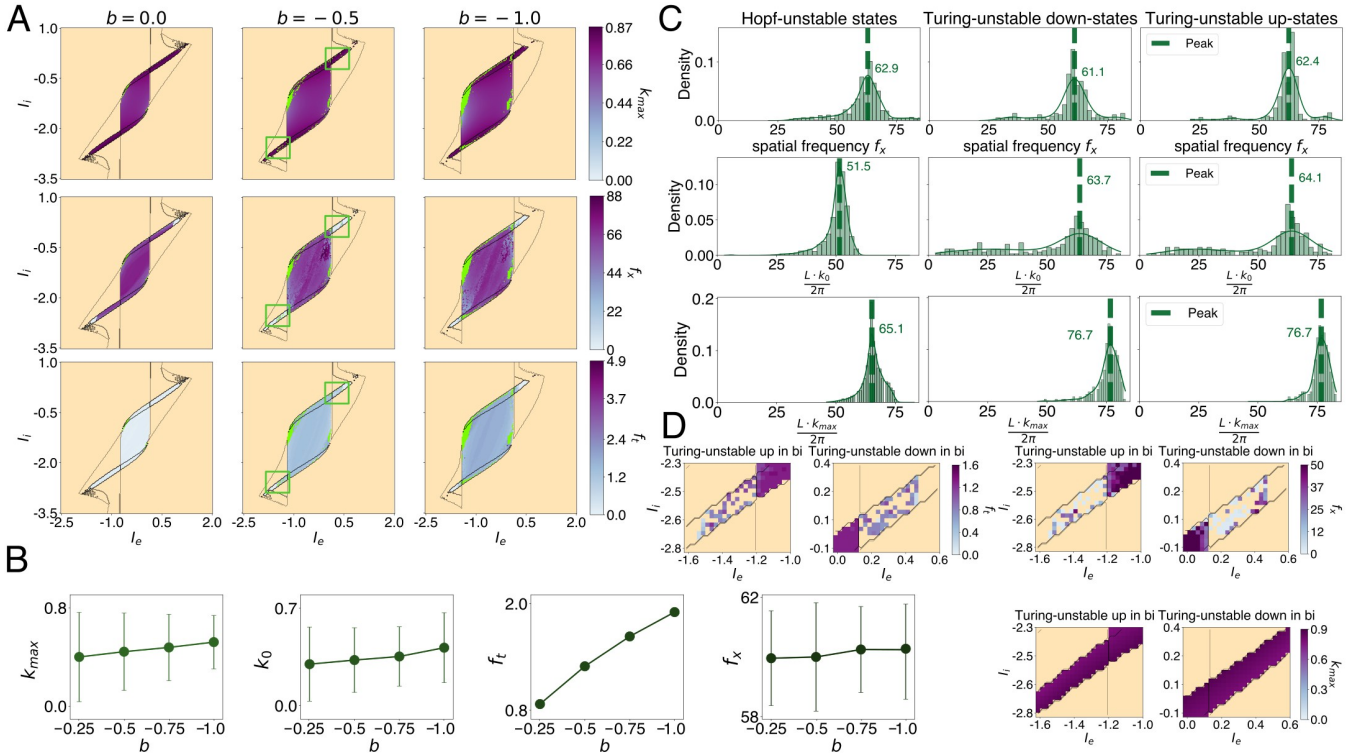


FIG. 5. Properties of the spatio-temporal patterns emerging in Hopf- and Turing-unstable states for increasing h-current strength. **A**  $k_{max}$  values (top row), dominant spatial frequency  $f_x$  (middle row), and dominant temporal frequency  $f_t$  (bottom row) for each location in state space. The figure shows slices of state space spanned by the external input  $(I_e, I_c) \in [-2.5, 2] \times [-3.5, 1]$  for  $b \in \{0, -0.5, -1.0\}$ . Purple colors denote the corresponding feature values. Darker colors indicate higher values, see color bar. Yellow denotes states of no spatio-temporal activity, light green denotes states with irregular patterns with a standard deviation  $r$  of the Kuramoto-order parameter of  $r > 10^{-2}$ . Thin lines denote the boundaries of the dynamical regimes shown in Fig. 2A. Green boxes correspond to the panels shown in D. **B** Mean (dots) and variance (bars) of  $k_{max}$ ,  $k_0$ ,  $f_t$ , and  $f_x$  for  $b \in \{-0.25, -0.5, -0.75, -1\}$  for the states located in the Hopf-unstable, Turing-unstable up-, and Turing-unstable down-state regimes, for regular spatio-temporal activity for which the standard deviation of the Kuramoto-order parameter over time and space was  $r \leq 10^{-2}$  (see Appendix B3). **C** Histograms and kernel density estimates (KDE; thin lines) of the numerically calculated spatial frequency ( $f_x$ ; top row), the spatial frequency corresponding to  $k_0$  ( $\frac{L \cdot k_0}{2\pi}$ ; middle row), and the spatial frequency corresponding to  $k_{max}$  ( $\frac{L \cdot k_{max}}{2\pi}$ ; bottom row) in the regimes of Hopf instability (left column), Turing instability in down-states (middle column), and Turing instability in up-states (right column) for  $b = -0.5$ . Dashed vertical lines with numbers denote the location of the peak of the KDE. **D** Close-ups of state space (see green boxes in A) with values for  $k_{max}$  (lower right),  $f_x$  (upper right), and  $f_t$  (upper left) in the Turing-unstable up- (left panels) and down-states (right panels) in bi. Yellow denotes states of no spatio-temporal activity or with irregular patterns with a standard deviation  $r$  of the Kuramoto-order parameter of  $r > 10^{-2}$ . The other colors denote feature values (see color bars). Wavenumbers were acquired as described in Section II B; spatial and temporal frequencies as described in the Appendices B1 and B2. Numerical simulations were conducted with initialization close to the corresponding unstable fixed points.

larger than 14 and smaller than 10 between the distributions of  $f_x$  and  $\frac{L \cdot k_0}{2\pi}$ .

Moreover, spatial frequencies in Hopf-unstable states often lie in between  $k_0$  and  $k_{max}$ , whereas for Turing-unstable states values are slightly below the spatial frequencies corresponding to  $k_0$  which likewise held for simulated example activity traces in Hopf- and Turing-unstable states. These findings confirm that there is a range of spatial modes whose properties the activity patterns can inherit (called *stability balloon* in [63]<sup>6</sup>). Since

we summarize fixed points stable at  $k = 0$  undergoing a Turing bifurcation at  $k_0 > 0$  under Turing-unstable states, we know that  $k_0$  is the smallest wavenumber at which the homogeneous equilibrium becomes unstable, i.e., determining the broadest wave. Nonetheless, we see that waves tend to converge to spatio-temporal patterns with a spatial frequency slightly below the expected frequency corresponding to the smallest wavenumber  $k_0$ , all

<sup>6</sup> In [63], a stability balloon describes a region in an  $(R, \vec{q})$  plane,

where  $R$  is a control parameter to take the system further away from the equilibrium and  $\vec{q}$  the wave vector effectively representing the wavenumber in a spatially one-dimensional ring.

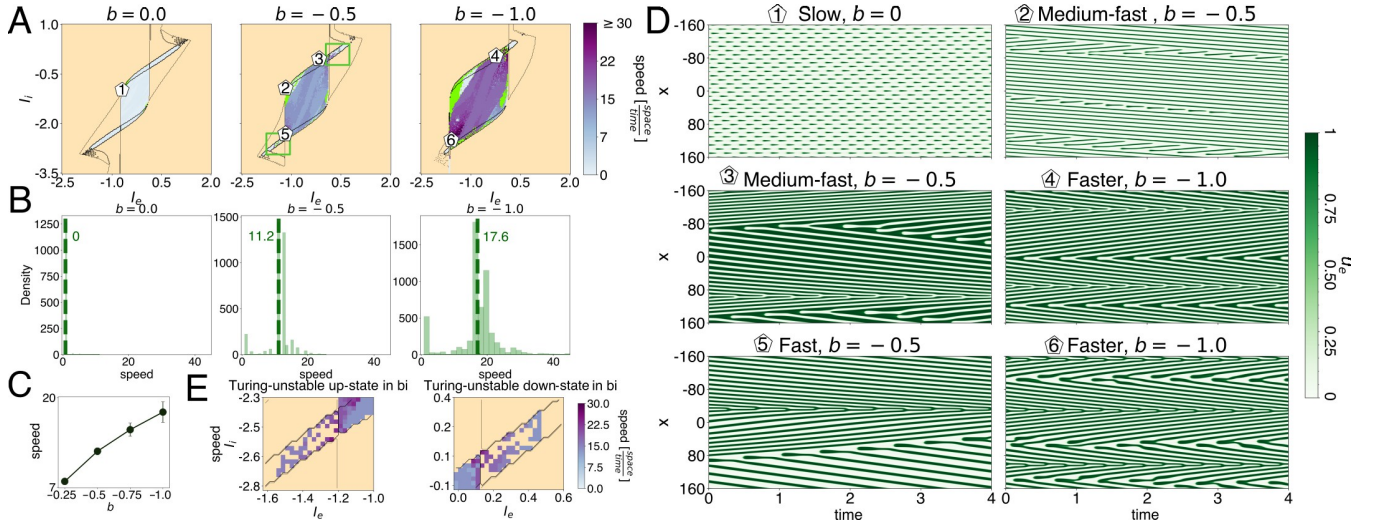


FIG. 6. Propagation speed of spatio-temporal patterns emerging in Hopf- and Turing-unstable states for increasing adaptation strength. **A** Slices of state space spanned by the external input currents showing speed values for the corresponding location in state space. Adaptation strength increases from left to right. Speed values are indicated by purple (see color bar), yellow denotes states of no spatio-temporal activity, green denotes states of irregular patterns with  $r > 10^{-2}$ . Thin lines denote the borders of the dynamical regimes shown in Fig. 2A. **B** Histograms of the distribution of speed values across the states shown in A. Dashed vertical lines and numbers denote the location of the peaks of the histograms. **C** Average (dots) and variance (bars) of speed values across state space for  $b \in \{-0.25, -0.5, -0.75, -1.0\}$ . **D** spatio-temporal patterns of  $u_e(x, t)$  for different values of  $b$  emerging in the locations in state space which are indicated by hexagons in A. The corresponding value of the external input currents are given in Table IV in Appendix B5. The corresponding speed values are for 1:  $< 0.5$ ; 2 and 3: 11.6; 4: 17.7; 5: 14.6; 6: 18.7. All other parameters are given in Table I. **E** Close-ups of state spaces (see green boxes in Fig. 6A) with values for speed. Numerical simulations were initialized around the fixed points of Hopf or Turing instability. Speed values were computed as described in Appendix B4.

the while the exact frequency varies depending on the initialization (see Appendix B7, Fig. 11).

Since we observe bistability in Hopf-unstable states between spatially homogeneous oscillations and temporally stationary spatial oscillations (see Section III, we performed the same analysis as in Figures 5A and D in Appendix B6 but initialized close to zero. Results are similar and shown in Appendix B6 Fig. 10. This figure also shows the  $k_0$  values over slices of state space corresponding to Fig. 5A.

Figure 5D shows close-ups of Turing unstable up- and down-states in bi for  $b = -0.5$ .  $k_{max}$  values do not deviate strongly from the  $k_{max}$  values of the rest of the considered state spaces but only few numerical simulations converged to regular spatio-temporal patterns (non-yellow locations in the close-ups of state space). The resulting patterns strongly depend on the initialization, and even initializations close to the Turing-unstable fixed point do not necessarily converge to a spatio-temporal pattern but to the coexisting stable fixed point, as exemplified in Fig. 2B, panel 5(\*), or irregular patterns<sup>7</sup>, as exemplified in Fig. 2B, panel 7. If regular spatio-temporal

patterns emerge, traveling waves show low values of spatial frequency. Temporal frequencies are also lower compared to the rest of state space.

To determine the propagation speed of adaptation-driven waves, we computed the phase velocity as described in Appendix B4 for each spatio-temporal activity pattern emerging in Turing- or Hopf-unstable states. Figure 6A shows the absolute value of the velocity, i.e., the *speed* for different locations in state space and for  $b \in \{0.0, -0.5, -1.0\}$ . Speed values increase, the larger  $|b|$  becomes. Toward the border of the regime of Hopf instability at which multiple different instability regimes meet (e.g., see region around hexagons 1 and 2), the activity patterns are either not regular (i.e.,  $r > 10^{-2}$ ) or not spatio-temporal (e.g.; purely spatial). Toward the regions of Turing instability in bi, speed increases (e.g., see darker colors around hexagon 6).

Figure 6B shows the distribution of speed values across Hopf-unstable and Turing-unstable states. The stronger the adaptation, the higher the speed values are. For  $b = 0$ , as expected, activity patterns do not travel across space (recall Fig. 2, panel 0) or their speed is  $< 0.5$  (see Fig. 6D, panel 1). For  $b = -0.5$ , there are two different speed values appearing the most often, with the dominant speed being 11.2. For  $b = -1$ , the variance of the distribution is larger and the most common speed value is once again higher at 17.6. Figure 6C confirms that the

<sup>7</sup> States marked in yellow in the regions of Turing-unstable up- and down-states in bi shown in Fig. 5D and Fig. 6E may also support regular spatio-temporal patterns if another initialization would have been chosen.

average speed across state space increases with adaptation strength. Figure 6D shows traveling waves for the same relative locations in state space (i.e., considering the shift to the left discussed in Section III), increasing in adaptation strength from left to right column. “Broad” patterns become “narrower”, increasing both temporal and spatial frequencies and their slope in the space-time diagrams, henceforth, the speed.

Figure 6E shows the same close-ups as Fig. 5D of Turing-unstable up- and down-states in bi showing the speed values for the numerical simulations converging to regular traveling waves. Speed values tend to be higher closer to the bifurcation line to the regime of single Turing-unstable up- and down-states.

## V. DISCUSSION

We implemented the adaptive Wilson-Cowan field model in a homogeneous setting with local connectivity on a one-dimensional spatial domain and periodic boundary conditions. Each position on the ring consists of an excitatory and an inhibitory population of neurons. The excitatory population is equipped with an adaptation mechanism that either corresponds to a hyperpolarizing negative feedback current (SFA) or a hyperpolarization-activated positive feedback current (h-currents). The parametrization used throughout this study was chosen to display multiple different phenomena which are also observed in the brain - from excitation-inhibition-driven faster oscillations, regimes of bistability, to spatio-temporal activity patterns that show SO-like dynamics as either adaptation mechanism is active.

We investigated the model system for increasing adaptation strength  $|b|$  only although the adaptation time constant  $\tau_m$  has an effect on the temporal dynamics of adaptation-driven traveling waves as well. The larger  $\tau_m$ , the lower the dominant temporal frequency becomes (results not shown, but see [44]) as has also been observed experimentally (see [64]). Changing the time constant scaled the eigenvalues for the different parameterizations explored. It had no effect on the dynamical landscape but could influence the bifurcation structure (results not shown). This is consistent with [43] who showed that for a reduced system,  $\tau_m$  determines whether a Turing bifurcation is dynamic or static.

A semi-analytical stability analysis across parameter space was performed for increasing adaptation strength resulting in the identification of over ten dynamical regimes including two types of bistability. Spatio-temporal patterns, most often periodic adaptation-driven traveling waves, emerge in states exhibiting Hopf and Turing instabilities if adaptation is sufficiently strong. Activity patterns remain stationary in the absence of adaptation which is explained by the zero imaginary part of all eigenvalues of the linearization matrix when a fixed point undergoes a Turing bifurcation. This aligns with the results presented in [43], who prove the existence

of stationary patterns for the reduced system if adaptation is sufficiently weak while traveling waves occur for stronger adaptation.

Changing the adaptation strength not only alters the model’s dynamical regimes but also the features of the emerging temporal and spatial patterns including the speed of traveling wave activity. The numerical simulations aligned with the mathematical analysis performed before. With stronger adaptation, wavenumbers increase on average, causing more waves on the ring, i.e., higher dominant spatial frequencies. Analogously, with growing imaginary parts of the eigenvalues at the zero crossing of their respective real parts for stronger adaptation, temporal frequencies also increase. These changes correlate with increasing traveling speeds of activity patterns when the adaptation becomes stronger.

Our results also show that the two adaptation mechanisms are mathematically equivalent when adaptation strength is compensated by a changed external input current. This is not a contradiction to the results of [21] who investigated SFA versus h-currents experimentally and using computational modeling. They identified differences between SFA and h-currents induced slow sequences of synchronized neuronal activity and sequential state transitions between up- and down-states. While a spatial gradient in the adaptation strength for SFA caused sequential down-state onsets and synchronized up-state onsets, h-currents replicated experimentally observed synchronized down-state onsets and sequential up-state initiation. Here, we show that the adaptation strength  $b$  has to be compensated by an additional external input to the excitatory population to preserve equivalency all the while adaptation induces and governs the emergent spatio-temporal properties. Consequently, a spatially heterogeneous adaptation strength (i.e.,  $b \rightsquigarrow b(x)$ ) will shape the emergent spatio-temporal activity patterns over space and break the equivalence between SFA and h-currents unless it is compensated by a spatially dependent external input  $I_e \rightsquigarrow I_e(x)$ .

In our population-based model, both adaptation mechanisms were implemented in a simplified way. Hyperpolarizing feedback current of somatic SFA can be mediated by potassium channels, which activate when the excitatory neurons are in a depolarized high-activity state, effectively causing  $K^+$  outward flow [11, 65]. Different potassium channels have different properties leading to differential effects in the actual adaptation mechanism: Voltage- ( $I_m$ , see [66]) and sodium-activated  $K^+$ -channels ( $I_{KNa}$ , see [67]) contribute mostly to subthreshold, while  $Ca^{2+}$ -activated  $K^+$ -channels ( $I_{KCa}$ , [68]) contribute to spike-based adaptation. Different channel types also have different effects on the response properties of a neuron, for example, on a neuron’s f-I curve when adaptation strength is increased [47]. In addition, SFA can be mediated by sodium current inactivation which cause the excited population of neurons to become less depolarized via the inactivation of  $Na^+$  inward flow [69]. That said, our SFA model appropriately captures their canon-

ical role as slow, hyperpolarizing feedback mechanisms which activate in an up-state. H-current based adaptation is mediated by a different channel dynamics, causing dichotomous effects. The responsible hyperpolarization-activated cyclic nucleotide gated (HCN) channels cause  $K^+$  outward flow, all the while not preventing  $Na^+$  inward flow [70], and have a reversal potential between -50 and -20 mV [15]. Unlike potassium channels who have a clear selection of  $K^+$  (see [71]), HCN channels have a permeability of 3:1 to 5:1 for  $K^+ : Na^+$  [15, 72, 73]. HCN channels are active as long as the neurons conductance is close to its resting membrane potential, causing positive inward currents that effectively excite the neuron. This, we simulate here, whereas the stagnating inhibitive effect for higher values of the membrane potential is neglected similar to the cortical population model of [21]. Clearly, dynamical equivalence between SFA and h-current based adaptation is only expected to strictly hold for the approximate description of the adaptation dynamics given by Eqs. (1) and (3).

For the reason of particularly addressing the influence of the dichotomy of the most prominent features of the adaptation mechanisms, we omitted delays, although it has been shown that delays can drive directions of waves in oscillator networks (see [74]) and enrich the emergent dynamics of complex spatio-temporal patterns (see [75]). Delays however would not affect the shown symmetry of the adaptation mechanisms.

Traveling waves of SOs are often presented as the propagation of alternating up- and down-states (see [36, 56]), in which one can separate the propagation of up-states via down-to-up transitions from the traveling of down-states via up-to-down transitions. In our model, we show that h-currents require less external input to the excitatory population than SFA to transition from a maintained stable down-state into oscillatory states, due to the shift of state space to the left along the  $I_e$ -axis. Note that even though we conduct simulations in a parameter space spanning negative values for external input currents, including thresholds in the transfer functions of the neuronal populations shifts the state space, exactly as is, along the axes of the external input currents by the value of the thresholds.

In the mean-field model with SFA of [45], the authors

show that SFA shifts the state space horizontally to the right along the axis of the external input to the excitatory population, which agrees with our results. Consequently, to simulate a maintained up-state activity that, either by transient or noisy inputs, allows temporal deactivation of the neuronal populations into a down-state (i.e., down-state onsets), requires more external input to the excitatory population. Additionally, we see in our state spaces that the opposite holds for h-currents, induced by the shift to the left. H-currents consequently require less external input both for up-state onsets as well as down-state onsets, and therefore, also lower transient inputs to maintain a slow alternation between up- and down-states.

Further studies could extend our investigations to a biophysically more realistic model, for example, as in [47], which distinguishes subthreshold activated versus spike-triggered SFA. [44] show for the model of [47] that subthreshold activated SFA changes the neuronal input-output relationship, and can increase the variability of interspike intervals (ISI) independent of current inputs, whereas spike-triggered SFA changes the ISIs variability based on the input to the neurons. It would be interesting to see, how far the diverse types of activations in SFA would break the shown symmetry to h-current based adaptation. For both adaptation mechanisms, the work of [22, 76] for non-spatial conductance based-models would allow to simulate other potentially symmetry-breaking channel dynamics, e.g., the stagnating inhibitive effect of h-currents. The Wilson-Cowan model investigated in this study may serve as a reference when exploring the effects of a biophysically realistic channel dynamics.

## ACKNOWLEDGMENTS

We thank Prof. Tilo Schwalger (Technische Universität Berlin) for very helpful comments and discussions. This work was funded by the Deutsche Forschungsgemeinschaft (DFG) as part of the CRC 1315 (project number 327654276). It was published on arXiv as a preprint in Oct. 2025 [77].

- 
- [1] M. V. Sanchez-Vives, M. Massimini, and M. Mattia, *Neuron* **94**, 993 (2017).
  - [2] M. V. Sanchez-Vives, *Current Opinion in Physiology* **15**, 217 (2020).
  - [3] M. Steriade, A. Nunez, and F. Amzica, *The Journal of Neuroscience* **13**, 3252 (1993).
  - [4] A. L. Loomis, E. N. Harvey, and G. Hobart, *Science* **82**, 198 (1935).
  - [5] S. Brodt, M. Inostroza, N. Niethard, and J. Born, *Neuron* **111**, 1050 (2023).
  - [6] J. G. Klinzing, N. Niethard, and J. Born, *Nature Neuroscience* **22**, 1598 (2019).
  - [7] B. Rasch and J. Born, *Physiological Reviews* **93**, 681 (2013).
  - [8] M. Massimini, R. Huber, F. Ferrarelli, S. Hill, and G. Tononi, *The Journal of Neuroscience* **24**, 6862 (2004).
  - [9] E. S. L. Faber and P. Sah, *The Neuroscientist* **9**, 181 (2003).
  - [10] G. Ha and E. Cheong, *Experimental Neurobiology* **26**, 179 (2017).
  - [11] D. A. McCormick, *Progress in Neurobiology* **39**, 337 (1992).

- [12] B. E. Jones, *Frontiers in Bioscience* **8**, s438 (2003).
- [13] T.-A. E. Nghiem, N. Tort-Colet, T. Górski, U. Ferrari, S. Moghimi-firoozabad, J. S. Goldman, B. Teleńczuk, C. Capone, T. Bal, M. di Volo, and A. Destexhe, *Cerebral Cortex* **30**, 3451 (2020).
- [14] D. Jercog, A. Roxin, P. Barthó, A. Luczak, A. Compte, and J. de la Rocha, *eLife* **6**, e22425 (2017).
- [15] C. L. Combe and S. Gasparini, *Progress in Biophysics and Molecular Biology* **166**, 119 (2021).
- [16] Y. Shu, A. Hasenstaub, and D. A. McCormick, *bioRxiv* 10.1101/2023.07.12.548753 (2023).
- [17] A. Destexhe and A. Babloyantz, *NeuroReport* **4** (1993).
- [18] A. Destexhe, D. A. McCormick, and T. J. Sejnowski, *Biophysical Journal* **65**, 2473 (1993).
- [19] S. Hill and G. Tononi, *Journal of Neurophysiology* **93**, 1671 (2005).
- [20] S. Y. Abbas, S. W. Ying, and P. A. Goldstein, *Neuroscience* **141**, 1811 (2006).
- [21] D. Mehrotra, D. Levenstein, A. J. Duszkievicz, S. S. Carrasco, S. A. Booker, A. Kwiatkowska, and A. Peyrache, *Current Biology* **34**, 3043 (2024).
- [22] L. Dalla Porta, A. Barbero-Castillo, J. Sanchez-Sanchez, N. Cancino, and M. V. Sanchez-Vives, *The Journal of Physiology* **603**, 2409 (2025).
- [23] P. C. Bressloff, *Journal of Physics A: Mathematical and Theoretical* **45**, 033001 (2011).
- [24] B. Ermentrout, *Journal of Computational Neuroscience* **5**, 191 (1998).
- [25] G. Ermentrout and D. Terman, *Mathematical Foundations of Neuroscience*, Interdisciplinary Applied Mathematics (Springer New York, 2010).
- [26] S. Budzinskiy, A. Beuter, and V. Volpert, *Chaos: An Interdisciplinary Journal of Nonlinear Science* **30**, 083144 (2020).
- [27] R. Erazo-Toscano and R. Osan, *Physical Review E* **107**, 034403 (2023).
- [28] O. E. Omel'chenko and C. R. Laing, *Physical Review E* **110**, 034411 (2024).
- [29] S. Coombes, *Waves, bumps, and patterns in neural field theories* (2005).
- [30] M. R. Qubbaj and V. K. Jirsa, *Physica D: Nonlinear Phenomena* **238**, 2331 (2009).
- [31] J. D. Harris and B. Ermentrout, *Physica D: Nonlinear Phenomena* **369**, 30 (2018).
- [32] J. Wyller, P. Blomquist, and G. T. Einevoll, *Physica D: Nonlinear Phenomena* **225**, 75 (2007).
- [33] H. R. Wilson and J. D. Cowan, *Biophysical Journal* **12**, 1 (1972).
- [34] C. Dimulescu, R. Strömsdörfer, A. Flöel, and K. Obermayer, *Frontiers in Network Physiology* **5** (2025).
- [35] D. Levenstein, G. Buzsáki, and J. Rinzel, *Nature Communications* **10**, 2478 (2019).
- [36] M. Torao-Angosto, A. Manasanch, M. Mattia, and M. V. Sanchez-Vives, *Frontiers in Systems Neuroscience* **15**, 10.3389/fnsys.2021.609645 (2021).
- [37] P. C. Bressloff, *Physical Review E* **82**, 051903 (2010).
- [38] H. R. Wilson and J. D. Cowan, *Kybernetik* **13**, 55 (1973).
- [39] D. J. Pinto and G. B. Ermentrout, *SIAM Journal on Applied Mathematics* **62**, 206 (2001).
- [40] S. Amari, *Biological Cybernetics* **27**, 77 (1977).
- [41] S. E. Folias and P. C. Bressloff, *SIAM Journal on Applied Dynamical Systems* **3**, 378 (2004).
- [42] Z. P. Kilpatrick and P. C. Bressloff, *Physica D: Nonlinear Phenomena* **239**, 547 (2010).
- [43] R. Curtu and B. Ermentrout, *SIAM Journal on Applied Dynamical Systems* **3**, 191 (2004).
- [44] M. Augustin, J. Ladenbauer, and K. Obermayer, *Frontiers in Computational Neuroscience* **7** (2013).
- [45] C. Cakan and K. Obermayer, *PLOS Computational Biology* **16**, e1007822 (2020).
- [46] C. Cakan, C. Dimulescu, L. Khakimova, D. Obst, A. Flöel, and K. Obermayer, *Frontiers in Computational Neuroscience* **15**, 10.3389/fncom.2021.800101 (2022).
- [47] J. Ladenbauer, M. Augustin, and K. Obermayer, *Journal of Neurophysiology* **111**, 939 (2014).
- [48] M. Mattia and M. V. Sanchez-Vives, *Cognitive Neurodynamics* **6**, 239 (2012).
- [49] F. C. Roth and H. Hu, *Nature Communications* **11**, 2248 (2020).
- [50] S. Rich, T. A. Valiante, and J. Lefebvre, *PLOS Computational Biology* **21**, e1013199 (2025).
- [51] M. D'Andola, B. Rebollo, A. G. Casali, J. F. Weinert, A. Pigorini, R. Villa, M. Massimini, and M. V. Sanchez-Vives, *Cerebral Cortex* **28**, 2233 (2017).
- [52] M. Dasilva, A. Camassa, A. Navarro-Guzman, A. Pazi-enti, L. Perez-Mendez, G. Zamora-López, M. Mattia, and M. V. Sanchez-Vives, *NeuroImage* **224**, 117415 (2021).
- [53] M. V. Sanchez-Vives and D. A. McCormick, *Nature Neuroscience* **3**, 1027 (2000).
- [54] Z. P. Kilpatrick, Wilson-cowan model, in *Encyclopedia of Computational Neuroscience*, edited by D. Jaeger and R. Jung (Springer New York, New York, NY, 2013) pp. 1–5.
- [55] L. Papadopoulos, C. W. Lynn, D. Battaglia, and D. S. Bassett, *PLOS Computational Biology* **16**, 1 (2020).
- [56] M. V. Sanchez-Vives, *Current Opinion in Physiology* **15**, 217 (2020).
- [57] T. Friedlander and N. Brenner, *Proc Natl Acad Sci U S A* **106**, 22558 (2009).
- [58] I. Timofeev, M. Bazhenov, T. Sejnowski, and M. Steriade, *Proceedings of the National Academy of Sciences of the United States of America* **99**, 9533 (2002).
- [59] H.-y. Chu and X. Zhen, *Acta Pharmacologica Sinica* **31**, 1036 (2010).
- [60] C. Ganguly, S. S. Bezugam, E. Abs, M. Payvand, S. Dey, and M. Suri, *Communications Engineering* **3**, 22 (2024).
- [61] D. A. McCormick and H. C. Pape, *J Physiol* **431**, 291 (1990).
- [62] Á. Byrne, D. Avitabile, and S. Coombes, *Physical Review E* **99**, 012313 (2019).
- [63] M. C. Cross and P. C. Hohenberg, *Reviews of Modern Physics* **65**, 851 (1993).
- [64] L. M. Giocomo and M. E. Hasselmo, *The Journal of Neuroscience* **28**, 9414 (2008).
- [65] A. Bhattacharjee and L. K. Kaczmarek, *Trends in Neurosciences* **28**, 422 (2005).
- [66] D. A. Brown and P. R. Adams, *Nature* **283**, 673 (1980).
- [67] P. C. Schwindt, W. J. Spain, and W. E. Crill, *Journal of Neurophysiology* **61**, 233 (1989).
- [68] D. A. Brown and W. H. Griffith, *The Journal of Physiology* **337**, 287 (1983).
- [69] C. M. Upchurch, C. L. Combe, C. J. Knowlton, V. G. Rousseau, S. Gasparini, and C. C. Canavier, *Journal of Neuroscience* **42**, 3768 (2022), epub 2022 Mar 24.
- [70] C.-H. Lee and R. MacKinnon, *Cell* **168**, 111 (2017), epub 2017 Jan 12.
- [71] A. Mironenko, U. Zachariae, B. L. de Groot, and

- W. Kopec, *Journal of Molecular Biology* **433**, 167002 (2021).
- [72] H.-C. Pape, *Annual Review of Physiology* **58**, 299 (1996).
- [73] M. Biel, C. Wahl-Schott, S. Michalakis, and X. Zong, *Physiological Reviews* **89**, 847 (2009).
- [74] R. C. Budzinski, T. T. Nguyen, G. B. Benigno, J. Doàn, J. Mináč, T. J. Sejnowski, and L. E. Muller, *Physical Review Research* **5**, 013159 (2023).
- [75] J. A. Roberts, L. L. Gollo, R. G. Abeyauriya, G. Roberts, P. B. Mitchell, M. W. Woolrich, and M. Breakspear, *Nature Communications* **10**, 1056 (2019).
- [76] M. Martin and M. G. Pedersen, *PLOS Computational Biology* **20**, e1011559 (2024).
- [77] R. Strömsdörfer and K. Obermayer, (2025), arXiv:2510.08436 [nlin.AO].
- [78] H. G. E. Meijer and S. Coombes, *Journal of Mathematical Biology* **68**, 1249 (2014).
- [79] D. Rubino, K. A. Robbins, and N. G. Hatsopoulos, *Nature Neuroscience* **9**, 1549 (2006).

## Appendix A

### 1. Analysis of the Wilson-Cowan model for zero and small values of $b$

In analogy to the full system discussed in Section II B, the linearized and Fourier-transformed ODE system without adaptation is given by

$$\begin{aligned}\tau_e \partial_t \hat{\Phi} &= -\hat{\Phi} + w_{ee} F'_e(B_e) \hat{w}_e \hat{\Phi} - w_{ei} F'_e(B_e) \hat{w}_i \hat{\Phi} \\ \tau_i \partial_t \hat{\varphi} &= -\hat{\varphi} + w_{ie} F'_i(B_i) \hat{w}_e \hat{\Phi} - w_{ii} F'_i(B_i) \hat{w}_i \hat{\varphi}.\end{aligned}\quad (\text{A1})$$

For  $\vec{X} = \begin{bmatrix} \hat{\Phi} \\ \hat{\varphi} \end{bmatrix}$ , Eqs. (A1) can be written in vector notation,

$$\partial_t \vec{X} = A(k) \vec{X}, \quad (\text{A2})$$

where

$$A_2(k) = \begin{bmatrix} \frac{1}{\tau_e} (-1 + w_{ee} F'_e(B_e) \hat{w}_e(k)) & -\frac{w_{ei}}{\tau_e} F'_e(B_e) \hat{w}_i(k) \\ \frac{w_{ie}}{\tau_i} F'_i(B_i) \hat{w}_e(k) & \frac{1}{\tau_i} (-1 - w_{ii} F'_i(B_i) \hat{w}_i(k)) \end{bmatrix}$$

$$B_l = w_{le} \tilde{u}_e - w_{li} \tilde{u}_i + I_l, \quad l \in \{e, i\},$$

and  $(\tilde{u}_e, \tilde{u}_i)$  denote the fixed point. Equations (A2) have solutions of the form  $[\hat{\Phi}, \hat{\varphi}]^T = \vec{r}(k) e^{i\lambda(k)t}$ , where  $\lambda(k) = \alpha(k) + i\omega(k)$  denotes an eigenvalue of  $A_2(k)$  for a given wavenumber  $k$ ,  $i$  the imaginary unit, and  $\vec{r}(k)$  the corresponding eigenvector. If the model system has a single fixed point which is unstable at  $k = 0$ , i.e., if there is at least one eigenvalue with  $\alpha(0) \geq 0$ , we call both the model system and the state of variables *Hopf-unstable*. Furthermore, if there is a wavenumber  $k_0 > 0$  for which at least one of the stability conditions

$$\begin{aligned}\det(A_2(k_0)) &> 0 \\ \text{tr}(A_2(k_0)) &< 0\end{aligned}$$

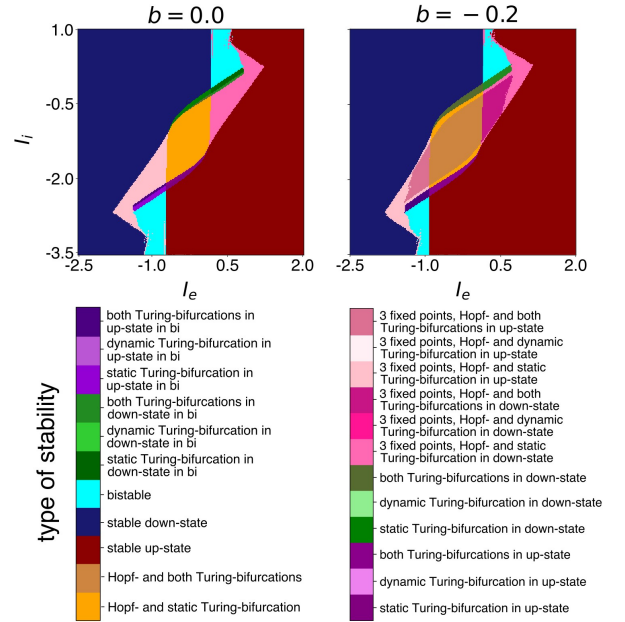


FIG. 7. State spaces over input pairs  $(I_e, I_i) \in [-2.5, 2] \times [-3.5, 1]$  for  $b \in \{0, -0.2\}$ . Colors denote the different types of bifurcations and the corresponding fixed point in which they occur (see color bar).

is violated, the fixed point  $(\tilde{u}_e, \tilde{u}_i)$  undergoes a Turing bifurcation. One can further distinguish *static* (i.e.,  $\alpha(k_0) = \omega(k_0) = 0$ ) and *dynamic* (i.e.,  $\alpha(k_0) = 0, \omega(k_0) \neq 0$ ) Turing instabilities (see [78]).

### 2. Static and dynamic Turing bifurcations for small values of $b$

Figure 7 shows the state spaces for  $b = 0$  and  $b = -0.2$  including the distinction of static vs. dynamic Turing bifurcations. Without adaptation, the system shows static Turing bifurcations. For a small value of  $b = -0.2$ , nearly all formerly static Turing bifurcations are either dynamic, or both dynamic and static Turing bifurcations occur at different non-zero wavenumbers as, for example, in Fig. 4, upper row, for  $b \neq 0$ , indicated by small arrows in panels below plots.

### 3. Activity traces for traveling and standing waves with finite adaptation

Figure 8 show the excitatory activity for very weak adaptation. While for  $b = -0.03$  the waves travel over space, they become stationary for  $b = -0.02$

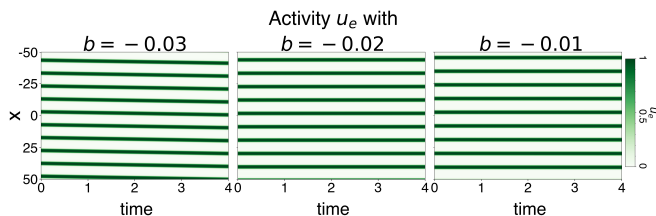


FIG. 8. Activity traces  $u_e(x, t)$  corresponding to the Turing-unstable down-state shown in Fig. 4, bottom row, for  $x \in [-50, 50]$ .

## Appendix B: Numerical Simulations and Feature Acquisition

### 1. Initialization and implementation

All models are implemented in python. The code is provided at <https://github.com/ronja-roevardotter/equivalent-adaptation-wilson-cowan-field.git><sup>8</sup>. The temporal integration is implemented using Runge-Kutta of the fourth order with an integration time step  $dt = 0.1$ . For the spatial convolution, we used the Fourier transform of `numpy`. For every parameterization, we conducted numerical simulations with two different initializations in fixed points that were either Hopf- or Turing-unstable. For random initialization, we sampled  $u_e(x, 0), u_i(x, 0), m(x, 0)$  for every position  $x$  on the ring from a uniform distribution  $\mathcal{U}(0, 0.001)$ . When initializing close to the fixed point value  $(\tilde{u}_e, \tilde{u}_i, \tilde{m})$ , additive noise was sampled from a normal distribution with standard deviation 0.1. For the latter, we conducted three simulations with three different seeds, to ensure that all results presented in this study were not an artefact of the particular seed used. All features (temporal and spatial frequencies, regularity, and speed of spatio-temporal patterns) that were investigated were computed for the excitatory activity traces  $u_e$ . We conducted numerical simulations with a duration of 30 time units and discarded the first 10 time units to reduce the effects of transients. To find fixed points and eigenvalues, the `scipy.optimize` package was used, making the analytical stability analysis semi-analytical. Numerical artifacts occur and were individually corrected whenever possible. However, some regions in state space remain „speckled“, which can be seen, for example, in the top right corners of the panels in Fig. 2A. In this numerically sensitive area in state space, the nullclines change from three intersections with a stable up- and down-state to three fixed points with one stable up-state and, finally, to one stable up-state when  $I_e$  and  $I_i$  are increased. The numerical approximation

methods do not always detect the fixed points correctly, leading to a few misclassifications of the state’s stability properties at these locations. To identify, how sensitive the linearization matrix, Eq. (6), and its eigenvalues are to deviations from the fixed point values for each location in state space, we added a small perturbation  $\xi = 10^{-8}$  to the fixed point values and computed the absolute difference of the resulting eigenvalues to the eigenvalues without  $\xi$ . We did so to ensure that the results of our stability analysis could be considered reliable. We found near-zero values for the most part of every state space with an increase in sensitivity values closer to bifurcation lines. Nonetheless, sensitivity values were always below  $10^{-5}$ .

### 2. Spatial and Temporal Frequencies

We define *one time unit* as  $unit_t = 10,000$  time-iteration steps and quantify temporal frequency by  $\left[\frac{\text{oscillation periods}}{unit_t}\right]$ . For brevity, we write  $\left[\frac{osc}{unit_t}\right]$ . This choice is based on the model’s ability to generate slow oscillations (i.e.,  $\leq 2 \frac{osc}{unit_t}$ ) for finite adaptation (i.e.,  $b \neq 0$ ) as well as faster oscillations (e.g.,  $\alpha$ -like oscillations with  $8 - 13 \frac{osc}{unit_t}$ ) that are generated by the excitatory-inhibitory loop (see, e.g.,  $f_t$  in Fig. 10A). To determine the dominant temporal frequency, we computed the power spectra  $P_{sx}(f)$  of the time series of the excitatory activity for each position  $x$ . Then we averaged over all positions,

$$\bar{P}_s(f) = \frac{1}{N} \sum_{x=1}^N P_{sx}(f),$$

and determined the frequency of maximum power of the averaged power spectrum, i.e.,  $f_s = \text{argmax}_f \bar{P}_s(f)$ . To characterize spatial oscillations, we computed the power spectrum over space  $P_{xt}(f)$  for each time step  $t \in [0, T \cdot unit_t]$ , where  $T = 20$  denotes the amount of times units used after discarding the transients (see Section B 1). Then, we averaged over all time steps,

$$\bar{P}_x(f) = \frac{1}{T \cdot unit_t} \sum_{t=1}^{T \cdot unit_t} P_{xt}(f),$$

and determined the spatial frequency of maximum power over the averaged power spectrum, i.e.,  $f_x = \text{argmax}_f \bar{P}_x(f)$ . For both temporal and spatial frequencies, activity patterns exist for which the power spectrum shows multiple peaks. In those cases we report the temporal and spatial frequencies corresponding to the most prominent peak.

### 3. Regularity of patterns

We characterized the spatio-temporal pattern using the Kuramoto-order parameter. We computed the ana-

<sup>8</sup> Within this framework, notebooks generating Figs. 1 and 4 are provided, allowing users to zoom in for a more detailed view.

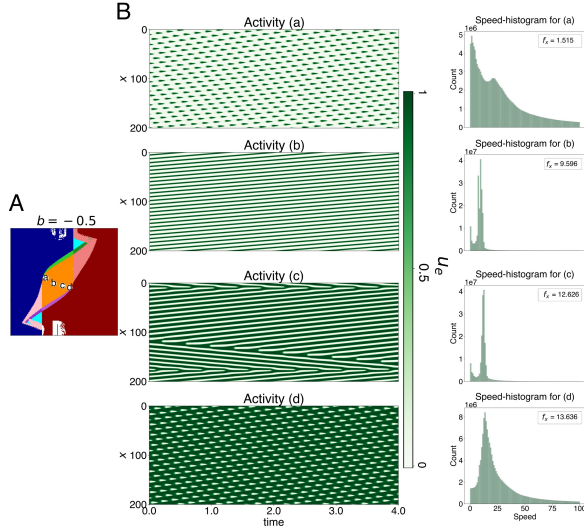


FIG. 9. Computation of dominant speed values. **A** Locations in state space for the activity patterns (a)-(d) shown in **B**. **B** Left panels: Activity traces for  $x \in [0, 200]$ . Green colors denote activity values (darker green for higher, lighter green for low activity, see color bar). Right panels: Corresponding histograms of local speed values. The dominant speed corresponds to the speed value occurring most often.

lytical signal representation of the activity  $u_e(x, t)$  using the Hilbert-Transform

$$z(x, t) = u_e(x, t) + i\mathcal{H}[u_e(x, t)], \quad (\text{B1})$$

where  $\mathcal{H}[\cdot]$  denotes the Hilbert-transformation and  $i$  the imaginary unit. Using the instantaneous phase

$$\theta(x, t) = \arctan\left(\frac{\text{Im}(z(x, t))}{\text{Re}(z(x, t))}\right) \quad (\text{B2})$$

we calculate the Kuramoto-order parameter  $R(t)$  for each time step  $t$

$$R(t) = \left| \frac{1}{n} \sum_x e^{i\theta(x, t)} \right|$$

and define the regularity  $r$  of a spatio-temporal pattern by its standard deviation

$$r = \sqrt{\frac{1}{T} \sum_{t=1}^T (R(t) - \bar{R})^2}, \quad \bar{R} = \frac{1}{T} \sum_{t=1}^T R(t)$$

over a time interval  $[0, T]$ . We considered patterns to be regular if  $r \leq 10^{-2}$ . This threshold corresponds to the mean over the ten most irregular patterns found when compiling Fig. 5A.

#### 4. Phase velocity and speed

To compute the speed in  $\left[\frac{\text{unit}_x}{\text{unit}_t}\right]$ , where  $\text{unit}_x = \frac{1}{dx}$ , of a spatio-temporal pattern, we used the approach of

[79]. We first determine the analytical representation of the activity  $u_e(x, t)$  as in Eq. (B1), where  $\theta(x, t)$  is the instantaneous phase at position  $x$  and time step  $t$  as in Eq. (B2). The local speed  $s(x, t)$  is computed from the temporal and spatial derivatives  $\frac{\partial \theta}{\partial x}(x, t)$  of the instantaneous phase,

$$s(x, t) = \left| \frac{\frac{\partial \theta(x, t)}{\partial t}}{\frac{\partial \theta(x, t)}{\partial x}} \right|.$$

Since spatio-temporal patterns may be composed of traveling waves of different speeds (e.g., see Fig. 6B, panel 5), we apply a similar approach as for the dominant spatial frequency. We compute a histogram over all local speed values appearing per activity pattern and take the speed value appearing the most often. In Fig. 9, we illustrate this procedure for four different activity patterns.

#### 5. Input pair tables for Figures 2 and 6

TABLE III. Input pairs  $(I_e, I_i)$  for Fig. 2.

Location	1	2	3	4	5	6
$I_e$	-0	-0.05	-0.5	-0.55	0.4	-0.55
$I_i$	-0.35	-1.6	-1.25	-0.425	0.2	-2

TABLE IV. Input pairs  $(I_e, I_i)$  for Fig. 6.

Location	1	2	3	4	5	6
$I_e$	-0.6	-0.85	-0.025	-0.275	-1.1	-1.35
$I_i$	-0.875	-0.875	-0.2	-0.2	-2.325	-2.325

#### 6. Visualization of feature-spaces with initialization close to zero

We conducted same analysis as for Figures 5A and 5C but with the activity variables initialized close to zero. Figure 10A shows the wavenumber  $k_0$  and the spatial,  $f_x$  (center row) and temporal,  $f_t$  (bottom row) frequencies for the spatial, temporal, and spatio-temporal patterns emerging in Turing- and Hopf-unstable states for increasing adaptation strength. We see that further away from the bifurcation lines, inside the regime of Hopf instability, purely temporal oscillations emerge with higher temporal frequencies compared to the activity patterns which emerge after initializing close to the Hopf-unstable fixed point. Closer to the bifurcation lines, purely spatial patterns emerge for  $b = 0$ , that become spatio-temporal for  $b \neq 0$ . Figure 10B shows the distribution of spatial frequencies of spatio-temporal patterns for  $b = -0.5$  compared to  $k_0$  and  $k_{max}$ . While the Wasserstein-distance is similar in value ( $\approx 12.5$ ) comparing the distributions of

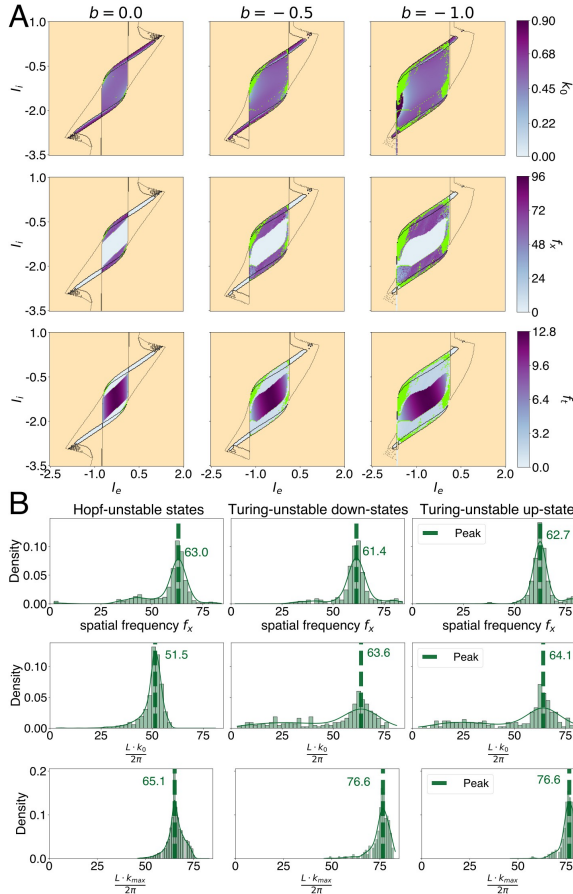


FIG. 10. Properties of the spatio-temporal patterns emerging in Hopf- and Turing-unstable states for increasing h-current strength. **A** Wavenumber  $k_0$  (top row), dominant spatial frequency  $f_x$  (middle row), and dominant temporal frequency  $f_t$  (bottom row) for each location in state space. The figure shows slices of state space spanned by the external input  $(I_e, I_e) \in [-2.5, 2] \times [-3.5, 1]$  for  $b \in \{0, -0.5, -1.0\}$ . Purple colors denote the corresponding feature values. Darker colors indicate higher values, see color bar. Yellow denotes states of no spatio-temporal activity, light green denotes states with irregular patterns with a standard deviation  $r$  of the Kuramoto-order parameter of  $r > 10^{-2}$ . Thin lines denote the boundaries of the dynamical regimes shown in Fig. 2A. **B** Histograms and kernel density estimates (KDE; thin lines) of the numerically calculated spatial frequency ( $f_x$ ; top row), the spatial frequency corresponding to  $k_0$  ( $\frac{L \cdot k_0}{2\pi}$ ; middle row), and the spatial frequency corresponding to  $k_{max}$  ( $\frac{L \cdot k_{max}}{2\pi}$ ; bottom row) in the regimes of Hopf instability (left column), Turing instability in down-states (middle column), and Turing instability in up-states (right column) for  $b = -0.5$ . Dashed vertical lines with numbers denote the location of the peak of the KDE. Numerical simulations were conducted with initializations close to zero.

$f_x$  and  $\frac{L \cdot k_{max}}{2\pi}$  in all three regions of state space, the most often appearing frequency again agrees best with  $\frac{L \cdot k_0}{2\pi}$  in Turing-unstable states and  $\frac{L \cdot k_{max}}{2\pi}$  in Hopf-unstable states. This is similar to what is observed for numerical simulations initialized close to the corresponding unstable fixed point.

## 7. Spatial frequencies of the spatio-temporal patterns emerging for different initializations

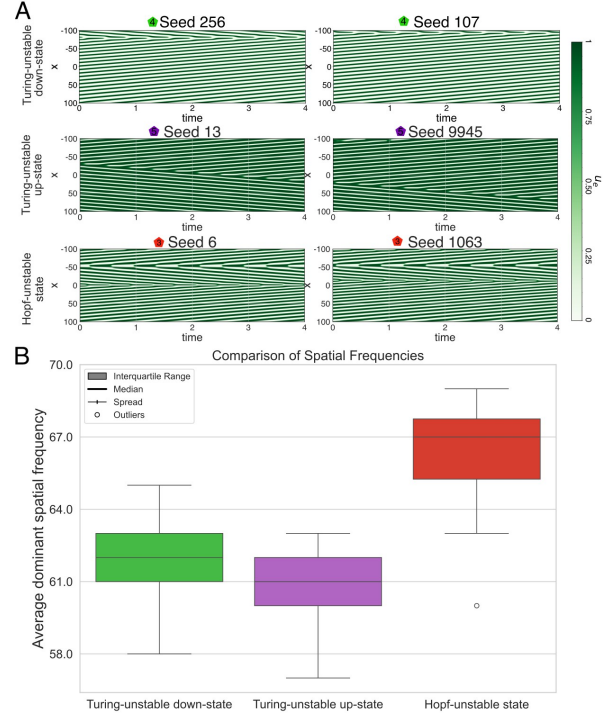


FIG. 11. **A** Activity traces 4, 6, and 3 (top to bottom row) of Fig. 2 initialized close to the fixed points of Turing instability in a down-state (first row), in an up-state (second row), and of Hopf instability but with different seeds. **B** Consistency of the spatial dynamics for 30 different seeds for each activity in A. Visualized are interquartile ranges (boxes), medians (horizontal lines inside boxes), spread (error bars), and outliers outside of spread (circles) for the Turing-unstable down-state (green) and up-state (purple), and the Hopf-unstable state (red).